Available online at www.sciencedirect.com

ScienceDirect

Geochimica et Cosmochimica Acta 152 (2015) 89–121

Geochimica et Cosmochimica Acta

www.elsevier.com/locate/gca

Petrogenesis of Late Cenozoic basalts from North Hainan Island: Constraints from melt inclusions and their host olivines

Jian-Qiang Liu [a,b], Zhong-Yuan Ren [a,*], Alexander R.L. Nichols [c], Mao-Shuang Song [a], Sheng-Ping Qian [a,d], Yan Zhang [a,d], Pei-Pei Zhao [a,d]

[a] *State Key Laboratory of Isotope Geochemistry, Guangzhou Institute of Geochemistry, Chinese Academy of Sciences, Guangzhou 510640, China*
[b] *State Key Laboratory for Mineral Deposits Research, School of Earth Sciences and Engineering, Nanjing University, 22 Hankou Road, Nanjing 210093, China*
[c] *Institute for Research on Earth Evolution (IFREE), Japan Agency for Marine Earth Science and Technology (JMSTEC), 2-5 Natsushima-cho, Yokosuka, Kanagawa 237-0061, Japan*
[d] *University of Chinese Academy of Sciences, Beijing 100049, China*

Received 17 March 2014; accepted in revised form 24 December 2014; Available online 9 January 2015

Abstract

Melt inclusions and their host olivines in basaltic lavas provide important information about the nature of their mantle source. We present the first analyzed chemical data of olivine-hosted melt inclusions in Cenozoic basalts from the North Hainan Island and report the discovery of both tholeiitic and alkalic melt inclusions in a single rock sample. Cenozoic basalts from the Hainan Island are predominantly tholeiites with only small amounts of alkali basalts. There is a much broader compositional variation in melt inclusions than whole rocks. Compared to partial melts of mantle peridotite, the Hainan basalts have lower CaO, Na_2O/TiO_2, CaO/Al_2O_3 and Co/Fe, and higher TiO_2, FeO^*, Fe/Mn, Zn/Fe and Zn/Mn. The olivine phenocrysts from the Hainan basalts contain lower Ca and Mn, and higher Ni and Fe/Mn than those of olivines crystallized from partial melts of peridotite. Projections from or towards olivine into the plane CS-MS-A for melt inclusions and whole rocks with MgO >7.5 wt% imply that the residual minerals in the source of the tholeiites are mainly clinopyroxene and garnet, possibly with some orthopyroxene, while in the source of the alkali basalts they are dominated by clinopyroxene and garnet. This indicates that a pyroxenite component could serve as the source lithology of the Hainan basalts. The OIB-like trace element compositions, with Ba, Sr, Nb and Ta positive anomalies, and Th and U negative anomalies, of the Hainan basalts suggest that a recycled oceanic crust component was involved in the source of the Hainan basalts. Based on a CMAS projection of primary magma compositions of the whole rocks and melt inclusions, we infer that a stage-2 silica-deficient pyroxenite derived from melt–peridotite reaction or mechanical mixing between recycled oceanic crust and peridotite can serve as the source lithology. Partial melts derived from such a source can match the overall compositions of the Hainan basalts better than those of MORB-eclogite and fertile peridotite. The compositional range from tholeiitic to alkalic basalts is ascribed to decreasing degrees of melting of a similar silica-deficient pyroxenite source, which is consistent with the lower incompatible trace element and REE abundances in the tholeiites compared to the alkali basalts. Both subalkaline and alkaline melt inclusions are present in a single sample, which indicates that magma mixing had occurred in the deep magma chamber prior to eruption below the Hainan Island.

1. INTRODUCTION

Identifying the petrology and mineralogy of the mantle source of basaltic lavas is a major challenge. For decades,

* Corresponding author at: Guangzhou Institute of Geochemistry, Chinese Academy of Sciences, Wushan, Guangzhou 510640, China. Tel.: +86 20 85292969; fax: +86 20 85290261.
E-mail address: zyren@gig.ac.cn (Z.-Y. Ren).

http://dx.doi.org/10.1016/j.gca.2014.12.023
0016-7037/

it was generally believed that mantle peridotite melt to produce basaltic magmas (Yoder and Tilley, 1962; Green and Ringwood, 1963; O'Hara and Yoder, 1967; Mckenzie and Bickle, 1988; McDonough and Sun, 1995; Putirka, 2005; Rhodes et al., 2012). However, recent studies have demonstrated that partial melts derived from volatile-free peridotite cannot closely reproduce the major element compositions of many intra-plate basalts (Hauri, 1996; Kogiso et al., 2003; Ren et al., 2004). Therefore, peridotite + CO_2 (Hirose, 1997; Dasgupta et al., 2007; Zeng et al., 2010), pyroxenite (this paper refers to generalized pyroxenite, including bimineralic eclogite) (Hauri, 1996; Hirschmann et al., 2003; Kogiso et al., 2003; Ren et al., 2004, 2006, 2009; Sobolev et al., 2005, 2007; Herzberg, 2006, 2011; Kogiso and Hirschmann, 2006; Jackson and Dasgupta, 2008), hornblendite (Pilet et al., 2004, 2008, 2011) and hybrid of peridotite with non-peridotite (Gao et al., 2004; Sobolev et al., 2005, 2007; Liu et al., 2008; Pilet et al., 2008) have been proposed as alternative mantle sources. Numerous isotope and trace element compositions of intra-plate ocean island basalts imply the presence of recycled oceanic crust in their mantle sources (Hofmann and White, 1982; Hauri, 1996; Hofmann, 1997; Lassiter and Hauri, 1998; Sobolev et al., 2000, 2005, 2007, 2008; Ren et al., 2005, 2006, 2009; Chauvel et al., 2007). Eclogite or pyroxenite formed by the reaction of recycled oceanic crust with peridotite has been identified as a significant component of the source region of intra-plate OIB (e.g., Hawaiian and Canary island) (Hauri, 1996; Sobolev et al., 2005, 2007, 2008; Ren et al., 2006, 2009; Herzberg, 2011; Mallik and Dasgupta, 2012). Lithospheric mantle metasomatized by carbonatitic or silicate melts has also been proposed to serve as the source of OIB in order to explain their enriched incompatible trace element and isotope characteristics (Halliday et al., 1995; Niu and O'Hara, 2003; Pilet et al., 2004, 2008; Workman et al., 2004).

Cenozoic continental intra-plate basalts are widespread in Southeast China, the South China Sea Basin and the Indo-China Peninsula (Zhou and Armstrong, 1982; Hoang et al., 1996; Chung et al., 1997; Zhou and Mukasa, 1997; Hoang and Flower, 1998; Ho et al., 2000, 2003; Zou et al., 2000; Fedorov and Koloskov, 2005; Yan et al., 2008; Zou and Fan, 2010; Wang et al., 2012, 2013; Fig. 1a), defining a potentially 'diffuse' igneous province in Southeast Asia (Hoang et al., 1996). These basalts show a wide spectrum of compositions from quartz tholeiites, through olivine tholeiites, to alkali olivine basalts and basanites (Hoang et al., 1996; Hoang and Flower, 1998; Ho et al., 2000, 2003; Wang et al., 2012). They are characterized by OIB-like incompatible trace element compositions (Chung et al., 1995, 1997; Hoang et al., 1996; Hoang and Flower, 1998; Ho et al., 2000, 2003; Zou and Fan, 2010; Wang et al., 2012). Their isotope compositions exhibit a Dupal-like Pb isotopic signature and mixing of DMM and EM2 components in their mantle source (Tu et al., 1991; Flower et al., 1992; Chung et al., 1994, 1995, 1997; Zhang et al., 1996; Zou et al., 2000; Fedorov and Koloskov, 2005; Han et al., 2009). A recent isotopic study of the Hainan basalts by Wang et al. (2013) indicates they have FOZO-like Sr, Nd, and Pb isotopic compositions, and identified an ancient mantle reservoir together with young recycled materials in their mantle source. Although abundant petrological and geochemical studies have been undertaken, the origin of these basalts is still a matter of debate, with a number of different interpretations having been proposed: (1) the tholeiites form by 8–9% partial melting of spinel lherzolite at depths of <66 km, while the alkali basalts derive from slightly lower degree (1–7%) partial melting of garnet lherzolite at >79 km (Fan and Hooper, 1991); (2) the tholeiites and alkali basalts originate from lithospheric mantle and asthenospheric mantle respectively (Hoang et al., 1996; Zhou and Mukasa, 1997; Hoang and Flower, 1998; Fedorov and Koloskov, 2005); (3) they were produced by the interaction between the lithosphere and asthenosphere (Chung et al., 1994, 1995; Ho et al., 2000, 2003; Han et al., 2009); or (4) that they were generated from the Hainan mantle plume (Lei et al., 2009; Zou and Fan, 2010; Wang et al., 2012, 2013).

It is worth noting that the previous work in this region was entirely based on the geochemical data of whole rocks. Yet, whole rocks are a 'mixture' of melts formed by a variety of complex processes involving source composition and partial melting in the mantle, mixing and blending of melts in shallow magma chambers, fractional crystallization and crustal contamination during their ascent. These processes can considerably reduce the diversity of bulk compositions and consequently often obscure the primary characteristics of the mantle sources (Sobolev, 1996; Sobolev et al., 2000; Hauri et al., 2002; Ren et al., 2005; Kent, 2008). In comparison to studies on whole rocks, melt inclusions provide additional information because they are trapped at higher pressure than eventual eruption. Firstly, they can preserve abundant volatile elements (H, C, Cl, S, F), which may be directly measured within trapped glasses. Secondly, they typically exhibit a higher degree of compositional diversity than whole rocks. Above all, they may also trap compositions that are more primitive than erupted lavas, approaching primary magma compositions. Thirdly, melt inclusions trapped within resistant minerals show that the inclusions can survive alteration by weathering, hydrothermal processes or low temperature metamorphism, providing the only means to directly establish the composition of magmatic liquids. Thus, melt inclusions are a powerful tool for the study of basaltic magma systems and their mantle source regions, and are widely used to study the origin and evolution of mafic lavas that may not always be available from whole-rock study (Sobolev, 1996; Kamenetsky and Crawford, 1998; Saal et al., 1998; Danyushevsky et al., 2000; Sobolev et al., 2000; Norman et al., 2002; Ren et al., 2005; Kent, 2008; Zhang et al., 2013).

In this study we present the chemical compositions of melt inclusions and their host olivines in Cenozoic basalts from the North Hainan Island, together with newly analyzed whole rock data. We use olivine-hosted melt inclusion geochemistry, combined with the whole rock geochemistry,

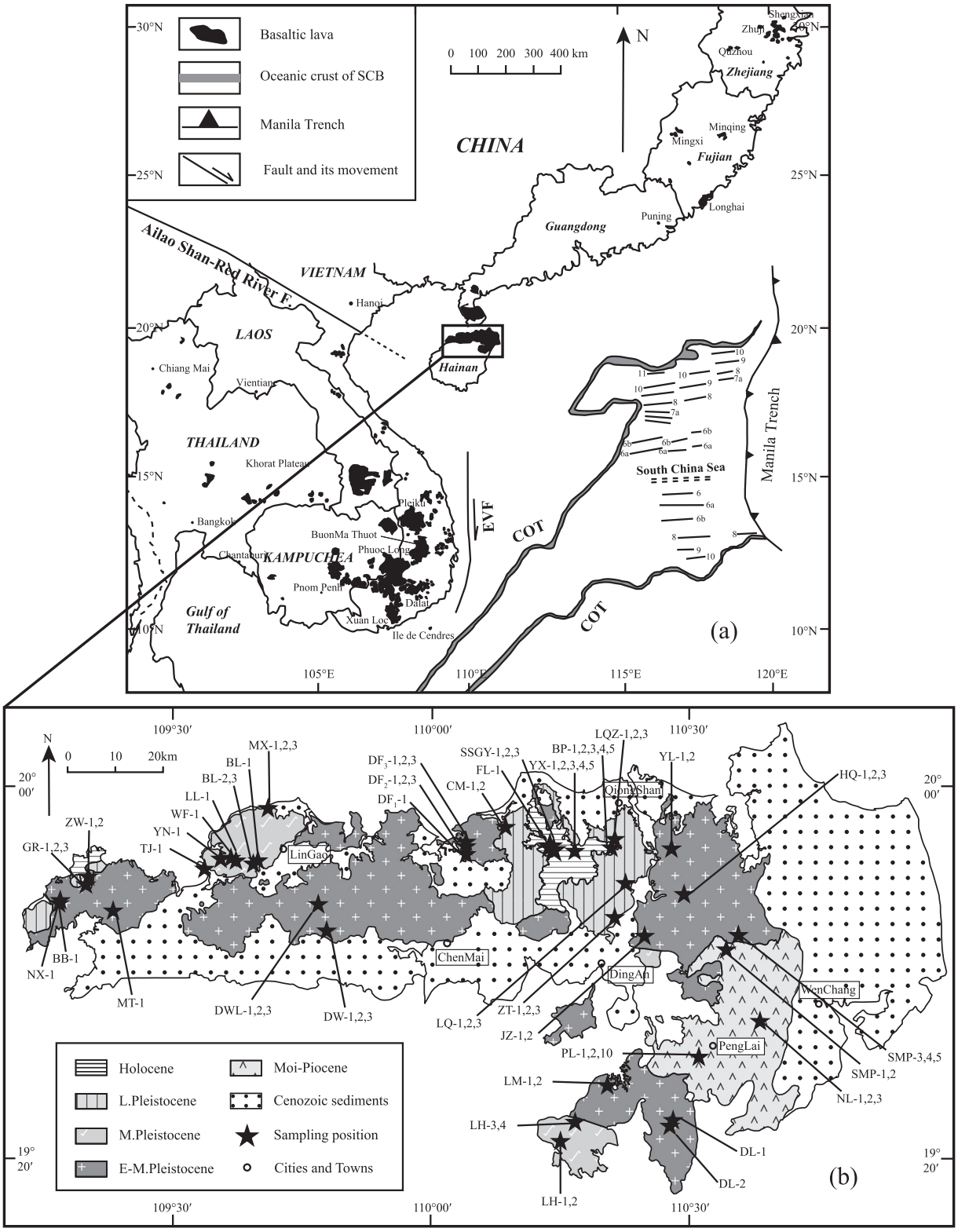

Fig. 1. (a) Sketch geological map of the Southeast China, South China Sea basin, Indo-China Peninsula and surrounding areas showing the spatial distribution of late Cenozoic intra-plate basaltic volcanism in the Southeast Asia (modified after Ho et al., 2003). (b) Distribution and sampling location of late Cenozoic basalts in North Hainan Island (modified after 2006–2008 measurements and revised geological map of Hainan province). Basalts are subdivided into five eruptive episodes according to their age data: Miocene–Pliocene, Early-Middle Pleistocene, Middle Pleistocene, Late Pleistocene and Holocene.

to constrain the source lithology of these basalts and discuss their petrogenesis. We discuss: (1) the effects of post-magmatic alteration on lava compositions; (2) the role of crystal fractionation and crustal contamination; (3) the nature and residual mineralogy of the magma source; and (4) the origin and magma mixing of the source region inferred from whole rocks and melt inclusions.

2. GEOLOGICAL BACKGROUND AND PETROGRAPHY

Hainan Island is in the southernmost tip of Mainland China. It is in the central area of the 'diffuse' igneous province of Southeast Asia (Fig. 1a). North Hainan Island is the largest area of Cenozoic basalts in Southeast China covering 4000 km^2 (Fig. 1b). The volcanism in Hainan Island began in the Late Oligocene (28.4 Ma), gradually increased in the Miocene and Pliocene (23–1.8 Ma), was most intense in the Pleistocene (1.8–0.012 Ma) and then gradually decreased before ceasing all together in the Holocene (<0.012 Ma) (Ho et al., 2000; Fan et al., 2004). Based on the timing of the South China Sea sea-floor extension (30–16 Ma, Chung et al., 1997; Sun et al., 2009), previous researchers considered that the Hainan basalts were mostly produced after the extension of South China Sea, with the highest eruption rate during the Pleistocene and Holocene (Flower et al., 1992; Ho et al., 2000, 2003). Assuming that ~5000 km^3 of magma was erupted from 50 to 20 ka, an eruption rate of 0.1–0.25 $km^3\ a^{-1}$ has been calculated for the Hainan basalts (Flower et al., 1992). This is on the same magnitude as the supply rates for flood basalts (Swanson, 1972; Cox, 1980). According to K–Ar and Ar–Ar dating of basaltic glass, stratigraphic contact relationship and lithologic characteristics, the Cenozoic basalts from Hainan Island can be subdivided into five eruptive episodes: Shimacun and Shimengou Formation in the Miocene–Pliocene, Duowen Formation in the Early-Middle Pleistocene, Dongying Formation in the Middle Pleistocene, Daotang Formation in the Late Pleistocene, and Shishan Formation in the Holocene (Ho et al., 2000; Fan et al., 2004; Long et al., 2006a, 2006b; Wang et al., 2012; Fig. 1b).

Eighty-two basaltic lavas were sampled from North Hainan Island, 68 of which were tholeiitic and 14 alkalic. The volcanic stratigraphy, rock types and locality of these samples are shown in Fig. 1b and Table 1. The tholeiites are aphyric to moderately phyric (<10%). Phyric tholeiites contain mostly olivine phenocrysts (3–10%), with few clinopyroxene phenocrysts (<1%). The olivine phenocrysts are euhedral to subhedral, 0.2–0.5 mm in size, and some are partially altered to low-temperature iddingsite. The groundmass is mainly composed of olivine, clinopyroxene, plagioclase, opaque minerals and glass. The alkali basalts are also phyric but contain more phenocrysts, with 5–7% olivine, approximately 7% clinopyroxene and 5–7% plagioclase. The olivine and plagioclase phenocrysts are euhedral to subhedral, while the clinopyroxene phenocrysts are anhedral. Olivine phenocrysts in both tholeiites and alkali basalts contain abundant melt inclusions, which are round or elliptical in shape, 30–150 μm in size and contain bubbles and also many clinopyroxene grains.

3. SAMPLE PREPARATION AND ANALYTICAL METHODS

The samples were sawed into thin slabs and the central fresh parts were chosen for analysis. The chosen slabs were wrapped in plastic foil and broken into chips, with the freshest chips chosen for bulk-rock chemical analysis and the remainder broken up further to separate olivine grains. The fresh chips were washed using deionized water in an ultrasonic bath three times for 20 min each time. Then they were crushed in a steel mortar to powders of ~200 mesh. Major element compositions of whole rocks were determined using a Rigaku ZSX-100e XRF instrument on glass disks at the State Key Laboratory of Isotope Geochemistry, Guangzhou Institute of Geochemistry, Chinese Academy of Sciences (GIGCAS). The analytical procedures followed were those in Goto and Tatsumi (1996). Analytical accuracy is better than 3% for SiO_2, Al_2O_3, Fe_2O_3, MgO, CaO, Na_2O and K_2O, and better than 5% for TiO_2, MnO and P_2O_5. Bulk rock trace element abundances were analyzed by Thermo Scientific XSERIES 2 inductively-coupled plasma-mass spectrometry (ICP-MS) at GIGCAS and the analytical accuracy is better than 5% for most of the trace elements (Liu et al., 1996).

Melt inclusions were prepared from selected grains at GIGCAS. Olivine grains were separated using a binocular microscope. To determine the chemical composition of the melt inclusion it is almost always preferable to analyze a homogeneous glass rather than a mixture of various crystalline phases and residual glass. Slowly cooled melt inclusions contain mixtures of crystals and glass and thus require reheating and quenching prior to analysis (Danyushevsky et al., 2000; Sobolev et al., 2000; Ren et al., 2005; Kent, 2008). In this study, the procedure of the homogenization and preparation processes of melt inclusions followed that described in Ren et al. (2005). We used a 1-atm gas-mixing furnace and kept the oxygen fugacity at the quartz-fayalite-magnetite buffer. Olivines from single sample were loaded into Pt capsules that were gradually lowered, over 10 min, from the top of the furnace (100 °C) to the hottest place in the furnace (1250 °C) and kept at that temperature for 10 min prior to quenching. Major element compositions of melt inclusions and olivines were analyzed by electron probe microanalysis (EPMA) with a JEOL JXA-8100 Superprobe at GIGCAS following the procedures of Sobolev et al. (2007) for olivines and Wang and Gaetani (2008) for melt inclusions. To monitor machine drift, an internal olivine standard (from Hannuoba mantle peridotite) and an internal glass standard (JB-2, Ren et al., 2004, 2005) were analyzed before and after each batch analysis. Olivines were analyzed using a 20 kV accelerating voltage, 300 nA beam current and 2 μm beam diameter. Repeated measurements on the internal olivine standard showed that the analytical uncertainty is better than 2% for SiO_2, FeO, MgO and MnO, 4% for NiO and 7% for CaO. The melt inclusions were analyzed using a 15 kV accelerating voltage, 200 nA beam current and 3 μm beam diameter. The volatile elements (Na, K) were analyzed first with peak counting times of 10 s and background counting time of 5 s. Repeated measurements on

Table 1
Sample localities and rock types of basaltic lavas from the North Hainan Island.

Sample	Eruptive episode	Eruption age	Locality	Rock type
YX-1	Shishan	Holocene	N 19°55′02.4″ E 110°15′57.9″	Alkali basalt
YX-2	Shishan	Holocene	N 19°55′02.4″ E 110°15′57.9″	Alkali basalt
YX-3	Shishan	Holocene	N 19°55′02.4″ E 110°15′57.9″	Trachybasalt
YX-4	Shishan	Holocene	N 19°55′02.4″ E 110°15′57.9″	Alkali basalt
YX-5	Shishan	Holocene	N 19°55′02.4″ E 110°15′57.9″	Trachybasalt
FL-1	Shishan	Holocene	N 19°55′34.1″ E 110°12′52.7″	Tholeiite
SSGY-1	Shishan	Holocene	N 19°55′39.6″ E 110°12′45.0″	Tholeiite
SSGY-2	Shishan	Holocene	N 19°55′39.6″ E 110°12′45.0″	Tholeiite
SSGY-3	Shishan	Holocene	N 19°55′39.6″ E 110°12′45.0″	Tholeiite
CM-1	Daotang	L.Pleistocene	N 19°57′24.8″ E 110°07′26.0″	Tholeiite
CM-2	Daotang	L.Pleistocene	N 19°57′24.8″ E 110°07′26.0″	Tholeiite
DF1-1	Duowen	E-M.Pleistocene	N 19°54′14.7″ E 110°02′28.0″	Tholeiite
DF2-1	Duowen	E-M.Pleistocene	N 19°54′42.6″ E 110°02′28.2″	Basaltic andensite
DF2-2	Duowen	E-M.Pleistocene	N 19°54′42.6″ E 110°02′28.2″	Basaltic andensite
DF2-3	Duowen	E-M.Pleistocene	N 19°54′42.6″ E 110°02′28.2″	Basaltic andensite
DF3-1	Duowen	E-M.Pleistocene	N 19°54′55.2″ E 110°02′28.9″	Basaltic andensite
DF3-2	Duowen	E-M.Pleistocene	N 19°54′55.2″ E 110°02′28.9″	Basaltic andensite
DF3-3	Duowen	E-M.Pleistocene	N 19°54′55.2″ E 110°02′28.9″	Basaltic andensite
DW-1	Duowen	E-M.Pleistocene	N 19°45′33.3″ E 109°46′11.7″	Basaltic andensite
DW-2	Duowen	E-M.Pleistocene	N 19°45′31.9″ E 109°46′12.0″	Basaltic andensite
DW-3	Duowen	E-M.Pleistocene	N 19°45′30.6″ E 109°46′13.1″	Basaltic andensite
DWL-1	Duowen	E-M.Pleistocene	N 19°47′30.5″ E 109°46′00.4″	Basaltic andensite
DWL-2	Duowen	E-M.Pleistocene	N 19°47′31.2″ E 109°46′01.3″	Alkali basalt
DWL-3	Duowen	E-M.Pleistocene	N 19°47′30.0″ E 109°46′04.3″	Trachybasalt
MX-1	Dongying	M.Pleistocene	N 19°59′39.8″ E 109°39′18.2″	Basaltic andensite
MX-2	Dongying	M.Pleistocene	N 19°59′39.8″ E 109°39′18.2″	Basaltic andensite
MX-3	Dongying	M.Pleistocene	N 19°59′39.8″ E 109°39′18.2″	Basaltic andensite
BL-1	Dongying	M.Pleistocene	N 19°52′46.0″ E 109°38′26.4″	Basaltic andensite
BL-2	Dongying	M.Pleistocene	N 19°52′41.1″ E 109°38′15.8″	Basaltic andensite
BL-3	Dongying	M.Pleistocene	N 19°52′40.5″ E 109°38′14.9″	Basaltic andensite
LQ-1	Daotang	L.Pleistocene	N 19°56′19.8″ E 110°20′53.8″	Basaltic andensite
LQ-2	Daotang	L.Pleistocene	N 19°56′19.8″ E 110°20′53.8″	Basaltic andensite
LQ-3	Daotang	L.Pleistocene	N 19°56′19.8″ E 110°20′53.8″	Basaltic andensite
LL-1	Dongying	M.Pleistocene	N 19°52′59.1″ E 109°35′41.1″	Basaltic andensite
WF-1	Dongying	M.Pleistocene	N 19°53′12.9″ E 109°35′10.3″	Basaltic andensite
GR-1	Shishan	Holocene	N 19°50′43.9″ E 109°17′29.9″	Trachyandensite
GR-2	Shishan	Holocene	N 19°50′43.7″ E 109°17′30.0″	Trachyandensite
GR-3	Shishan	Holocene	N 19°50′43.4″ E 109°17′30.2″	Trachyandensite
MT-1	Duowen	E-M.Pleistocene	N 19°47′58.3″ E 109°20′59.6″	Basaltic andensite
TJ-1	Dongying	M.Pleistocene	N 19°51′54.6″ E 109°31′42.4″	Basaltic andensite
YN-1	Dongying	M.Pleistocene	N 19°53′06.4″ E 109°34′01.0″	Basaltic andensite
ZW-1	Shishan	Holocene	N 19°51′18.8″ E 109°17′34.6″	Basaltic trachyandensite
ZW-2	Shishan	Holocene	N 19°51′18.8″ E 109°17′34.6″	Basaltic trachyandensite
BB-1	Duowen	E-M.Pleistocene	N 19°48′17.8″ E 109°13′55.2″	Basaltic andensite
NX-1	Duowen	E-M.Pleistocene	N 19°48′27.7″ E 109°13′55.0″	Basaltic andensite
BP-1	Shishan	Holocene	N 19°55′17.5″ E 110°20′39.8″	Tholeiite
BP-2	Shishan	Holocene	N 19°55′17.5″ E 110°20′39.8″	Alkali basalt
BP-3	Shishan	Holocene	N 19°55′17.5″ E 110°20′39.8″	Tholeiite
BP-4	Shishan	Holocene	N 19°55′15.8″ E 110°20′40.4″	Trachybasalt
BP-5	Shishan	Holocene	N 19°55′15.8″ E 110°20′40.4″	Tholeiite
LQZ-1	Daotang	L.Pleistocene	N 19°51′03.1″ E 110°21′51.0″	Basaltic andensite
LQZ-2	Daotang	L.Pleistocene	N 19°51′03.1″ E 110°21′51.0″	Basaltic andensite
LQZ-3	Daotang	L.Pleistocene	N 19°51′01.9″ E 110°21′51.4″	Basaltic andensite
JZ-1	Duowen	E-M.Pleistocene	N 19°45′03.2″ E 110°24′14.2″	Tholeiite
JZ-2	Duowen	E-M.Pleistocene	N 19°45′03.2″ E 110°24′14.2″	Tholeiite
ZT-1	Daotang	L.Pleistocene	N 19°46′56.6″ E 110°20′04.0″	Tholeiite
ZT-2	Daotang	L.Pleistocene	N 19°46′56.6″ E 110°20′04.0″	Tholeiite
ZT-3	Daotang	L.Pleistocene	N 19°46′56.6″ E 110°20′04.0″	Tholeiite
HQ-1	Duowen	E-M.Pleistocene	N 19°49′35.0″ E 110°28′57.5″	Basaltic andensite
HQ-2	Duowen	E-M.Pleistocene	N 19°49′35.0″ E 110°28′57.5″	Basaltic andensite

(*continued on next page*)

Table 1 (*continued*)

Sample	Eruptive episode	Eruption age	Locality	Rock type
HQ-3	Duowen	E-M.Pleistocene	N 19°49′35.0″ E 110°28′57.5″	Basaltic andensite
YL-1	Duowen	E-M.Pleistocene	N 19°54′39.6″ E 110°27′16.2″	Basaltic andensite
YL-2	Duowen	E-M.Pleistocene	N 19°54′39.6″ E 110°27′16.2″	Basaltic andensite
SMP-1	Shimacun	Miocene-Pliocene	N 19°43′39.3″ E 110°34′24.5″	Basaltic andensite
SMP-2	Shimacun	Miocene-Pliocene	N 19°43′37.7″ E 110°34′25.0″	Basaltic andensite
SMP-3	Duowen	E-M.Pleistocene	N 19°44′59.1″ E 110°35′44.8″	Basaltic andensite
SMP-4	Duowen	E-M.Pleistocene	N 19°44′59.1″ E 110°35′44.8″	Basaltic andensite
SMP-5	Duowen	E-M.Pleistocene	N 19°44′56.9″ E 110°35′44.6″	Basaltic andensite
NL-1	Shimacun	Miocene-Pliocene	N 19°34′10.1″ E 110°38′15.7″	Tholeiite
NL-2	Shimacun	Miocene-Pliocene	N 19°34′10.1″ E 110°38′15.7″	Basaltic andensite
NL-3	Shimacun	Miocene-Pliocene	N 19°34′06.6″ E 110°38′10.7″	Tholeiite
PL-1	Shimacun	Miocene-Pliocene	N 19°31′04.8″ E 110°30′38.6″	Tholeiite
PL-2	Shimacun	Miocene-Pliocene	N 19°31′04.8″ E 110°30′38.6″	Basaltic andensite
PL-10	Shimacun	Miocene-Pliocene	N 19°31′04.8″ E 110°30′38.6″	Tholeiite
DL-1	Duowen	E-M.Pleistocene	N 19°23′35.1″ E 110°28′12.9″	Tholeiite
DL-2	Duowen	E-M.Pleistocene	N 19°23′04.1″ E 110°27′44.4″	Tholeiite
LH-1	Dongying	M.Pleistocene	N 19°21′39.4″ E 110°14′18.9″	Tholeiite
LH-2	Dongying	M.Pleistocene	N 19°21′39.4″ E 110°14′18.9″	Tholeiite
LH-3	Dongying	M.Pleistocene	N 19°23′43.1″ E 110°15′33.5″	Tholeiite
LH-4	Dongying	M.Pleistocene	N 19°23′43.1″ E 110°15′33.5″	Tholeiite
LM-1	Duowen	E-M.Pleistocene	N 19°28′36.0″ E 110°19′41.1″	Tholeiite
LM-2	Duowen	E-M.Pleistocene	N 19°28′36.0″ E 110°19′41.1″	Tholeiite

L.Pleistocene – Late Pleistocene, M.Pleistocene – Middle Pleistocene, E-M.Pleistocene – Early-Middle Pleistocene.

the internal glass standard (JB-2) demonstrated that the analytical uncertainty is better than 0.5% for most major elements (except 6% for MnO and 8% for P_2O_5).

4. RESULTS

4.1. Major element compositions of whole rocks and melt inclusions

Bulk rock major element compositions of 82 Hainan basalts are listed in Table 2. According to the classification of Le Bas et al. (1986), the Hainan samples consist of both subalkaline and alkaline series. The subalkaline samples are mainly basaltic andesite and basalt, while the alkaline samples are principally basalt and trachybasalt with several extremely evolved trachyandesites and basaltic trachyandesites (Fig. 2).

The major element compositions of 386 olivine-hosted melt inclusions were analyzed from nine samples (six tholeiites and three alkali basalts) by EPMA. Melt inclusion compositions may be changed after entrapment, in which case they will not represent the original compositions (Danyushevsky et al., 2000, 2002; Kent, 2008). These changes can be driven by crystallization of the host mineral on the inclusion walls or the crystallization of other daughter phases within the inclusion prior to eruption. Such processes have been experimentally reversed by remelting and homogenizing melt inclusions. In addition, during natural cooling, melt inclusions can re-equilibrate with their host crystal. This re-equilibration process, called "Fe-loss", mostly results in significantly higher MgO and lower FeO^T contents within the olivine-hosted melt inclusion population (Danyushevsky et al., 2000), and cannot be reversed experimentally. There is a weak negative correlation between FeO contents of melt inclusions and Fo values of host olivines for all nine samples (Fig. 3a, b, c, g, h, i, m, n, o), indicating that Fe-loss has occurred in the melt inclusions. Furthermore, though with some scatter, the CaO/Al_2O_3 is nearly constant with decreasing Fo for respective melt inclusions (Fig. 3d, e, f, j, k, l, p, q, r), suggesting that they only experienced olivine fractionation, and clinopyroxene and plagioclase fractionation are insignificant. Hence the measured data are corrected for the Fe-loss using the method by Danyushevsky et al. (2000) and recalculated to be in equilibrium with the host olivines applying the model of Ford et al. (1983) using the PETROLOG software (Danyushevsky, 2001). This calculation requires an independent estimate of the initial trapped melt FeO^* content, which in most cases uses the FeO^* fractionation trend exhibited by the whole rocks (Danyushevsky et al., 2000, 2002). According to the FeO^* fractionation trend of the whole rocks, we set 10.5 wt% and 11 wt% of the total FeO as the initial trapped melt of tholeiites and alkali basalts, respectively.

The compositions of melt inclusions after "Fe-loss" correction are listed in Table A.1 and displayed on the TAS diagram (Fig. 2). The melt inclusions exhibit a wider compositional range than the whole rocks for both tholeiites and alkali basalts (Fig. 2), and tholeiitic and alkali basaltic melt inclusions are even present in the same rock sample (Fig. 4a, b, c, d). Fig. 5 shows that MgO contents of the melt inclusions are slightly lower than that of the whole rocks for both tholeiites and alkali basalts, indicating that their host olivines probably crystallized later in more evolved magmas. Combining the geochemical data of whole rocks with those of melt inclusions, it is clear

Table 2
Bulk rock major element compositions (in wt%) of Hainan basalts.

Sample	SiO_2	TiO_2	Al_2O_3	$Fe_2O_3^T$	MnO	MgO	CaO	Na_2O	K_2O	P_2O_5	LOI	Total
YX-1	48.36	2.29	12.17	12.08	0.15	11.28	8.37	2.60	1.76	0.48	−0.01	99.54
YX-2	48.36	2.27	12.13	12.03	0.15	11.19	8.41	2.79	1.75	0.47	−0.01	99.54
YX-3	49.92	2.87	13.78	11.65	0.14	6.47	8.47	3.23	2.36	0.64	−0.01	99.54
YX-4	49.73	2.61	13.66	11.46	0.14	7.38	9.09	2.91	2.01	0.55	0.00	99.54
YX-5	49.47	2.47	13.57	11.17	0.14	7.32	9.36	3.54	1.99	0.53	−0.01	99.54
FL-1	50.70	2.37	14.23	11.09	0.14	6.70	8.90	3.29	1.66	0.45	0.00	99.54
SSGY-1	51.21	2.34	14.03	10.96	0.14	6.63	8.96	3.11	1.71	0.43	−0.01	99.54
SSGY-2	50.40	2.39	14.38	11.19	0.14	6.78	9.17	3.09	1.55	0.44	0.00	99.54
SSGY-3	51.07	2.36	14.13	11.02	0.14	6.65	8.98	3.09	1.66	0.44	−0.01	99.54
CM-1	50.51	2.00	13.85	11.85	0.14	8.04	8.51	2.97	1.31	0.36	−0.01	99.54
CM-2	50.69	2.05	13.90	11.86	0.14	7.88	8.47	2.84	1.33	0.37	−0.01	99.54
DF_1-1	51.61	2.16	14.23	10.98	0.14	6.68	8.90	3.02	1.43	0.39	−0.01	99.54
DF_2-1	53.16	1.87	13.77	11.23	0.14	7.21	8.26	2.68	0.95	0.26	0.00	99.54
DF_2-2	53.13	1.88	13.70	11.31	0.14	7.30	8.22	2.67	0.92	0.27	0.00	99.54
DF_2-3	53.21	1.91	13.72	11.29	0.14	7.04	8.19	2.82	0.94	0.27	0.00	99.54
DF_3-1	52.96	1.90	13.61	11.38	0.14	7.30	8.15	2.89	0.95	0.27	0.00	99.54
DF_3-2	53.24	1.91	13.73	11.26	0.14	7.07	8.28	2.67	0.98	0.27	0.00	99.54
DF_3-3	53.03	1.90	13.67	11.29	0.14	7.19	8.17	2.93	0.96	0.27	0.00	99.54
DW-1	53.05	1.71	14.22	12.16	0.15	6.14	8.65	2.76	0.53	0.19	0.00	99.54
DW-2	52.97	1.59	14.48	11.95	0.15	6.30	8.60	2.86	0.46	0.18	0.00	99.54
DW-3	53.00	1.69	14.45	12.20	0.15	6.12	8.54	2.72	0.48	0.19	0.00	99.54
DWL-1	53.26	1.66	14.35	11.95	0.14	6.13	8.62	2.72	0.51	0.19	0.00	99.54
DWL-2	48.62	3.07	13.36	12.41	0.16	7.86	8.40	3.07	1.91	0.69	−0.01	99.54
DWL-3	48.64	3.05	13.47	12.41	0.15	7.67	8.19	3.30	1.96	0.70	0.00	99.54
MX-1	53.46	1.61	14.52	11.29	0.14	6.42	8.67	2.75	0.50	0.18	0.00	99.54
MX-2	53.41	1.71	14.28	11.85	0.15	6.00	8.61	2.80	0.52	0.19	0.00	99.54
MX-3	53.27	1.64	14.36	11.48	0.15	6.40	8.68	2.93	0.46	0.18	0.00	99.54
BL-1	53.27	1.64	14.62	11.69	0.14	6.30	8.51	2.71	0.47	0.18	0.00	99.54
BL-2	53.49	1.63	14.52	11.22	0.14	6.38	8.69	2.79	0.49	0.18	0.00	99.54
BL-3	53.17	1.65	14.40	11.65	0.14	6.32	8.70	2.81	0.51	0.18	0.00	99.54
LQ-1	52.56	1.59	14.37	11.49	0.14	7.07	8.52	2.69	0.89	0.22	0.00	99.54
LQ-2	52.79	1.63	14.16	11.59	0.14	6.92	8.39	2.74	0.95	0.23	0.00	99.54
LQ-3	52.56	1.59	14.18	11.35	0.14	6.88	8.44	3.19	0.99	0.23	0.00	99.54
LL-1	53.24	1.60	14.39	11.61	0.14	6.43	8.65	2.81	0.49	0.18	0.00	99.54
WF-1	53.48	1.67	14.44	11.49	0.14	6.14	8.70	2.83	0.47	0.18	0.00	99.54
GR-1	54.47	1.63	14.77	9.41	0.10	5.58	5.28	4.55	3.23	0.51	0.00	99.54
GR-2	54.42	1.65	14.79	9.39	0.10	5.49	5.23	4.68	3.29	0.51	0.00	99.54
GR-3	54.44	1.65	14.68	9.53	0.10	5.61	5.33	4.43	3.25	0.51	0.00	99.54
MT-1	51.88	1.84	13.85	11.89	0.14	7.32	8.09	3.08	1.12	0.33	0.00	99.54
TJ-1	53.32	1.60	14.55	11.51	0.14	6.40	8.60	2.78	0.47	0.17	0.00	99.54
YN-1	53.33	1.58	14.48	11.53	0.15	6.44	8.66	2.76	0.44	0.17	0.00	99.54
ZW-1	51.50	1.98	14.15	10.86	0.12	6.88	6.80	4.15	2.59	0.50	−0.01	99.54
ZW-2	51.47	1.98	14.19	10.93	0.12	6.95	6.80	4.04	2.55	0.50	−0.01	99.54
BB-1	52.11	1.84	14.16	11.48	0.13	6.62	7.80	3.48	1.54	0.36	0.00	99.54
NX-1	52.02	1.81	14.23	11.53	0.13	6.84	7.72	3.40	1.50	0.36	0.00	99.54
BP-1	49.11	2.07	13.15	11.55	0.15	9.66	9.11	2.89	1.46	0.40	−0.01	99.54
BP-2	48.88	2.05	13.11	11.50	0.15	9.66	9.05	3.28	1.47	0.39	−0.01	99.54
BP-3	49.19	2.11	13.22	11.59	0.15	9.54	9.12	2.76	1.47	0.40	−0.01	99.54
BP-4	48.71	2.05	13.00	11.47	0.14	9.60	9.03	3.64	1.51	0.39	−0.01	99.54
BP-5	49.13	2.05	13.22	11.51	0.15	9.75	9.28	2.66	1.43	0.38	−0.01	99.54
LQZ-1	52.81	1.58	14.08	11.54	0.14	7.02	8.49	2.79	0.87	0.22	0.00	99.54
LQZ-2	52.84	1.59	14.11	11.59	0.14	7.02	8.47	2.68	0.87	0.22	0.00	99.54
LQZ-3	52.57	1.59	13.99	11.53	0.14	6.96	8.44	3.16	0.91	0.24	0.00	99.54
JZ-1	51.15	2.04	13.55	12.40	0.13	7.42	8.56	2.80	1.13	0.35	0.00	99.54
JZ-2	51.00	2.03	13.66	11.81	0.15	7.89	8.64	2.77	1.23	0.35	0.00	99.54
ZT-1	50.75	1.89	13.54	12.39	0.15	8.29	8.47	2.72	1.06	0.29	−0.01	99.54
ZT-2	50.74	1.87	13.38	12.32	0.15	8.30	8.40	2.99	1.09	0.29	−0.01	99.54
ZT-3	50.69	1.87	13.44	12.27	0.15	8.17	8.40	3.15	1.12	0.29	−0.01	99.54
HQ-1	52.71	1.81	14.05	11.76	0.14	7.00	8.64	2.65	0.56	0.22	0.01	99.54
HQ-2	52.94	1.77	14.11	11.62	0.14	6.85	8.54	2.73	0.61	0.23	0.01	99.54

(*continued on next page*)

Table 2 (*continued*)

Sample	SiO_2	TiO_2	Al_2O_3	$Fe_2O_3^T$	MnO	MgO	CaO	Na_2O	K_2O	P_2O_5	LOI	Total
HQ-3	52.71	1.79	14.06	11.64	0.14	6.86	8.58	2.86	0.63	0.25	0.01	99.54
YL-1	52.33	1.76	14.29	11.77	0.14	7.13	8.67	2.60	0.58	0.24	0.01	99.54
YL-2	52.75	1.76	14.05	11.68	0.14	7.02	8.59	2.64	0.67	0.24	0.01	99.54
SMP-1	53.24	1.77	14.18	11.41	0.15	6.40	8.46	2.72	0.93	0.27	0.01	99.54
SMP-2	52.20	1.86	13.74	12.13	0.14	7.24	8.46	2.82	0.72	0.23	0.01	99.54
SMP-3	51.81	1.83	13.64	11.95	0.15	7.80	8.71	2.68	0.73	0.24	0.00	99.54
SMP-4	52.08	1.85	14.67	11.74	0.16	5.92	9.30	2.80	0.77	0.25	0.02	99.54
SMP-5	51.85	1.88	13.67	12.01	0.15	7.45	8.67	2.86	0.74	0.26	−0.01	99.54
NL-1	50.92	1.91	13.76	11.42	0.15	8.37	8.50	3.16	0.97	0.36	0.02	99.54
NL-2	52.06	1.88	13.83	11.31	0.14	7.46	8.69	3.10	0.76	0.29	0.01	99.54
NL-3	50.78	1.93	13.74	11.41	0.15	7.94	8.54	3.52	1.12	0.39	0.01	99.54
PL-1	50.98	1.63	13.61	11.19	0.14	9.72	8.45	2.68	0.88	0.27	0.00	99.54
PL-2	52.04	2.06	13.88	11.02	0.14	7.66	8.58	2.81	1.03	0.32	0.01	99.54
PL-10	48.43	1.70	12.46	11.56	0.15	12.62	7.95	3.30	1.03	0.33	0.02	99.54
DL-1	51.71	2.01	13.66	11.79	0.15	7.65	8.05	2.81	1.37	0.35	0.00	99.54
DL-2	51.16	2.00	13.53	12.02	0.15	7.51	8.03	3.45	1.33	0.35	0.00	99.54
LH-1	51.54	2.28	14.35	11.26	0.14	6.44	8.37	3.18	1.54	0.43	−0.01	99.54
LH-2	51.54	2.28	14.36	11.23	0.14	6.40	8.41	3.23	1.54	0.43	−0.01	99.54
LH-3	51.29	2.13	13.86	11.37	0.14	7.58	8.30	2.98	1.48	0.39	−0.01	99.54
LH-4	51.42	2.19	13.96	11.32	0.14	7.20	8.33	3.03	1.54	0.41	−0.01	99.54
LM-1	50.54	2.03	13.35	12.12	0.20	8.08	8.69	2.83	1.33	0.37	0.01	99.54
LM-2	49.98	1.99	13.11	12.83	0.19	8.29	8.69	2.82	1.28	0.36	0.01	99.54

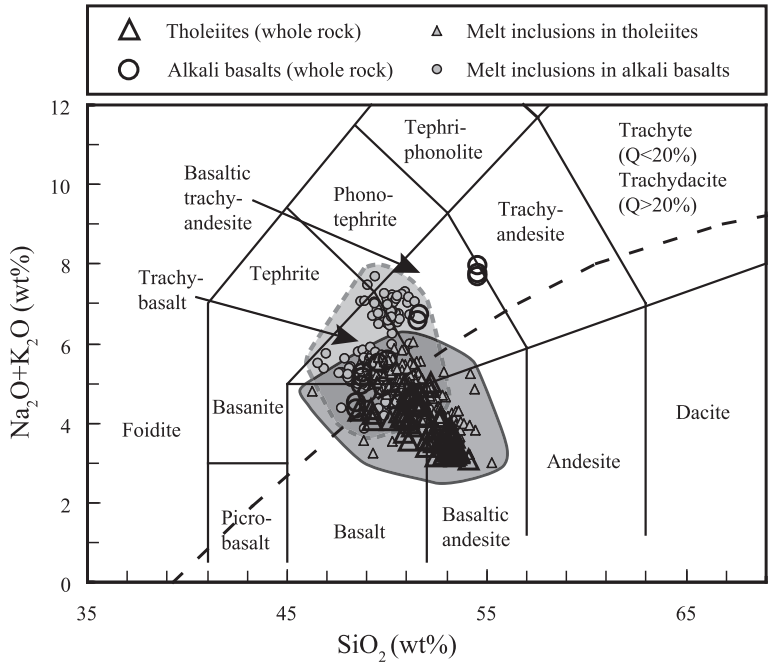

Fig. 2. $Na_2O + K_2O$ versus SiO_2 (Le Bas et al., 1986) for Hainan basalt whole rocks and melt inclusions. The compositions of melt inclusions have been corrected for Fe-loss using the software of Danyushevsky et al. (2000) (see text for further explanation). The solid gray area defines melt inclusions in tholeiites and the dashed gray area defines melt inclusions in alkali basalts. Melt inclusions exhibit wider compositional range than whole rocks.

that the tholeiites have higher SiO_2 and Al_2O_3 contents, but lower Na_2O, K_2O and TiO_2 contents than the alkali basalts (Fig. 5a, b, c, g, h). For the tholeiites, SiO_2 and Al_2O_3 contents correlate negatively, and Ni contents correlate positively, with MgO (Fig. 5a, c, i). TiO_2, CaO, Na_2O, Sc contents correlate slightly negatively with MgO (Fig. 5b, e, g, j), and there is no evident correlation between K_2O contents and MgO (Fig. 5h). Lastly, the FeO^T and CaO/Al_2O_3 remain nearly constant with decreasing MgO contents (Fig. 5d, f), holding the approximate ranges between 10 wt% and 11 wt% for FeO^T and between 0.55 wt% and 0.7 wt% for CaO/Al_2O_3 respectively

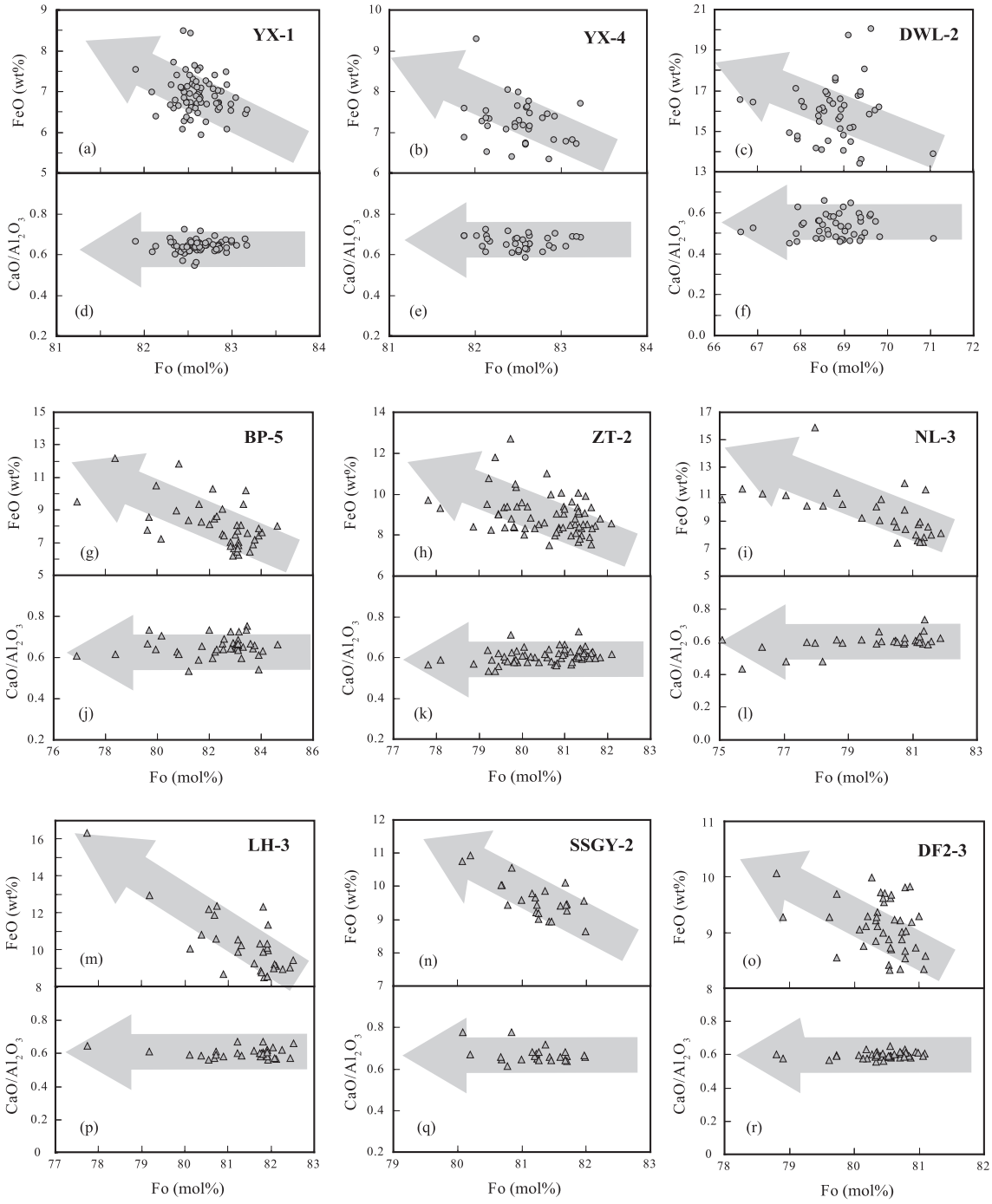

Fig. 3. (a), (b), (c), (g), (h), (i), (m), (n) and (o) show the relationship of FeO contents of Hainan melt inclusions (without correction) against Fo of their host olivines. There is a slight negative correlation between FeO and Fo for all of the tholeiites and alkali basalts, which indicates that Fe-loss has occurred in the melt inclusions. (d), (e), (f), (j), (k), (l), (p), (q) and (r) show the relationship of CaO/Al_2O_3 of melt inclusions (without correction) against Fo of their host olivines. CaO/Al_2O_3 remains constant with falling Fo for respective melt inclusions, suggesting that they only experienced olivine fractionation prior to eruption.

and defining a single olivine-controlled liquid line of descent (LLD). As for the alkali basalts, Al_2O_3, Na_2O and K_2O contents correlate negatively with MgO (Fig. 5c, g, h). At MgO >7.5 wt%, TiO_2, CaO and Sc contents correlate slightly negatively with MgO, and FeO^T and CaO/Al_2O_3 do not vary with decreasing MgO. However, at MgO <7.5 wt%, TiO_2, FeO^T, CaO, Sc and CaO/Al_2O_3 all decrease with MgO (Fig. 5b, d, e, f, j). SiO_2 contents correlate negatively with MgO, yet the slope is more abrupt when MgO <7.5 wt% (Fig. 5a). Likewise, Ni

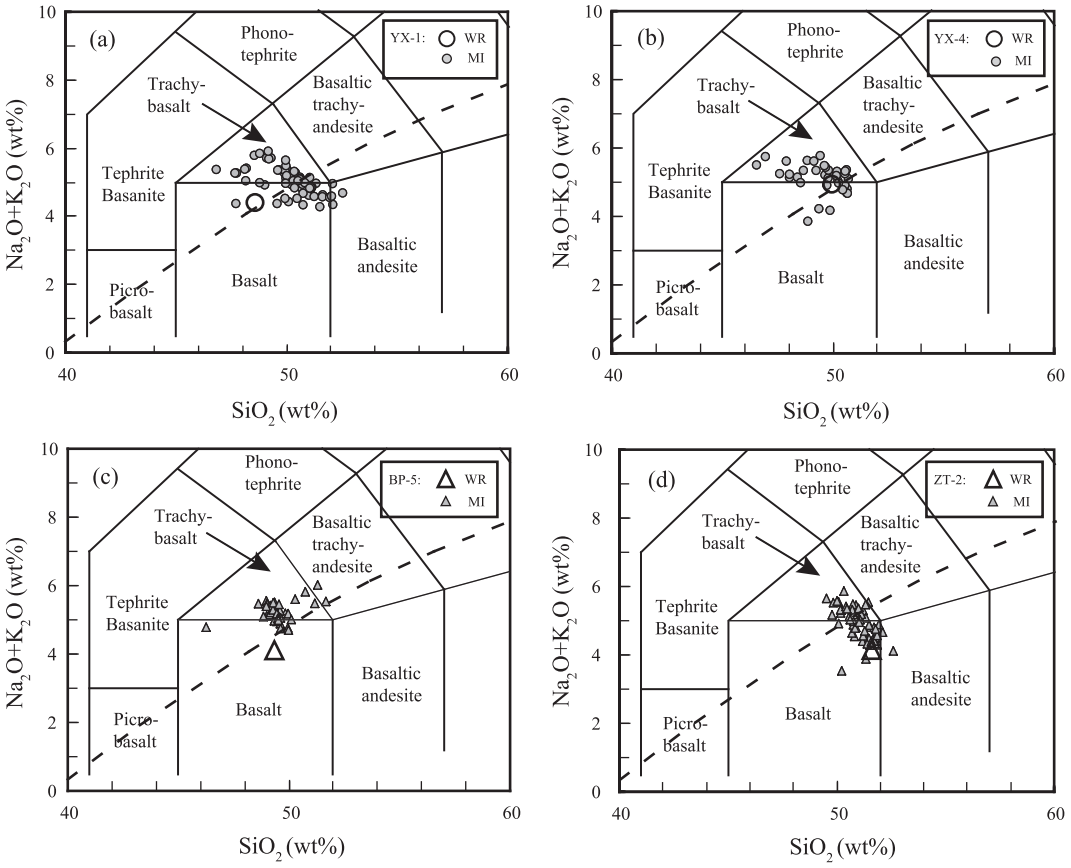

Fig. 4. $Na_2O + K_2O$ versus SiO_2 (Le Bas et al., 1986) for melt inclusions in a single rock sample and their whole rocks. Sample number is given in legend. WR denotes whole rock and MI melt inclusion. Tholeiitic and alkalic melt inclusions are present in single alkalic (a and b) and tholeiitic (c and d) rock samples, which suggests that magma mixing has occurred in the magma chamber prior to eruption beneath Hainan Island.

contents correlate positively with MgO, yet the slope is more gentle when MgO <7.5 wt% (Fig. 5i).

4.2. REE and other trace elements

Trace element analyses are listed in Table 3. As a whole, the tholeiites have lower REE and incompatible trace element contents than the alkali basalts (Figs. 6 and 7). ∑REE of the tholeiites is 66.2–158.0 ppm, with an average value of 106.1 ppm, while that of the alkali basalts is 128.8–233.6 ppm, with a mean value of 187.3 ppm. Chondrite-normalized REE patterns of the tholeiites and alkali basalts (Fig. 6a, b) reveal that all the studied samples are enriched in light rare earth elements (LREE) over high rare earth elements (HREE), typical of OIB. However, the tholeiites ($(La/Yb)_N = 3.85–14.7$, $(Ce/Yb)_N = 3.32–10.9$) display a smaller fractionation between LREE and HREE than the alkali basalts ($(La/Yb)_N = 10.6–44.1$, $(Ce/Yb)_N = 8.14–32.0$). In the primitive mantle-normalized incompatible trace elements spidergrams (Fig. 6 c, d), the tholeiites and alkali basalts exhibit similar patterns, with positive Rb, Ba, Nb–Ta and Sr anomalies, and negative Th and U anomalies. However, only the alkali basalts ($Ti/Ti^* = 0.87 \pm 0.32$) display weak negative Ti anomalies ($Ti/Ti^* = 1.00 \pm 0.14$ for the tholeiites). Such incompatible trace element patterns are similar to those of Enriched Mantle 2 (EM2), which is consistent with their isotopic compositions, but distinct from those of continental crust (negative Nb–Ta anomaly), N-MORB (depleted in LILE with a negative Sr anomaly) and Enriched Mantle 1 (EM1, highly enriched in LREE). Abundances of Rb, Ba, Th, U, La and Sr on the whole correlate well with Zr (Fig. 7), with the tholeiites having lower incompatible element concentrations than the alkali basalts.

4.3. Olivine composition

We analyzed the major element compositions of 628 olivines by EPMA, including 461 olivines from eight tholeiites and 167 olivines from three alkali basalts, (see Table A.2). These olivines have a wide range of compositions: Fo (69.4–84.6), MnO (0.151–0.277 wt%), NiO (0.153–0.334 wt%), CaO (0.032–0.29 wt%) for the tholeiites and Fo (66.6–83.2), MnO (0.164–0.365 wt%), NiO (0.097–0.292 wt%), CaO (0.204–0.3 wt%) for the alkali basalts. CaO contents show a negative correlation with Fo, and almost all of the olivines have CaO between 0.174 wt% and 0.3 wt% (except seven olivines from NL-3 with an average value of 0.03 wt%), which are higher than that of mantle xenoliths (CaO <0.1 wt%, Thompson and Gibson,

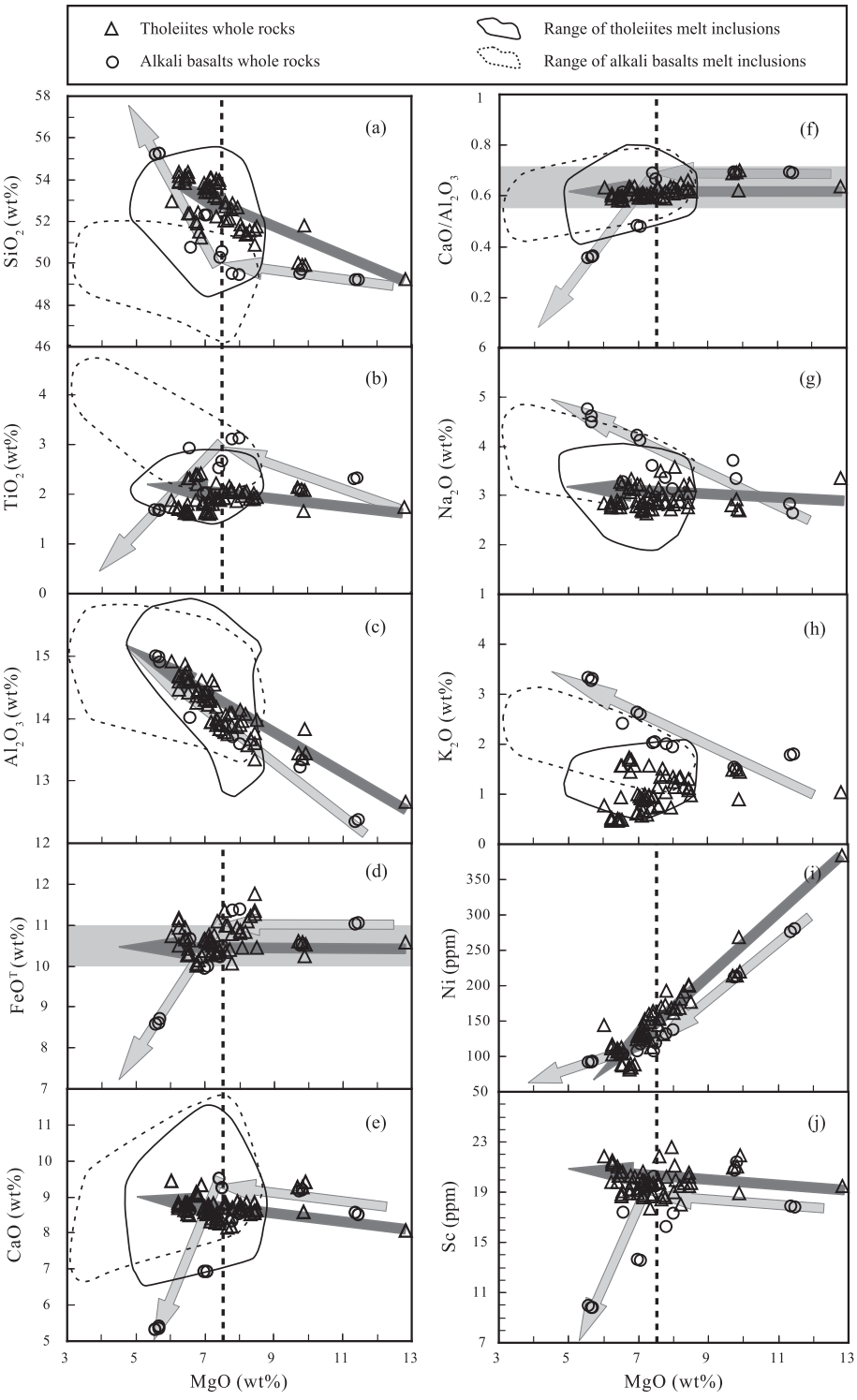

Fig. 5. Variation of SiO_2, TiO_2, Al_2O_3, FeO^T, CaO, CaO/Al_2O_3, Na_2O, K_2O, Ni, Sc versus MgO for the Hainan basalt whole rocks and melt inclusions measured in this study. The solid and dashed lines define the ranges of tholeiitic and alkalic melt inclusions respectively. The dark gray arrows show the trends of tholeiitic whole rocks while the light gray arrows indicate the trends of alkalic whole rocks. These relationships suggest that alkali basalts with MgO >7.5 wt% and all tholeiites only experienced fractionation of olivine, whereas clinopyroxene and plagioclase, and even Fe–Ti oxides had started to fractionate from alkali basalts with MgO <7.5 wt% (see text for further explanation).

2000; Ren et al., 2004; Fig. 8a). NiO contents decrease with Fo, as expected if the melt they are crystallizing from is undergoing fractional crystallization (Fig. 8b). These lines of evidence are consistent with the olivines crystallizing from magma system rather than being mantle-derived xenocrysts.

Table 3
Trace element concentrations (ppm) of Hainan basalts.

Sample	YX-1	YX-2	YX-3	YX-4	YX-5	FL-1	SSGY-1	SSGY-2	SSGY-3	CM-1	CM-2	DF1-1
Sc	17.8	17.84	17.35	19.49	20.23	19.75	19.26	20.24	18.92	19.5	19.01	20.3
Ti	13962	13904	18102	16751	15878	14333	14344	15033	13952	12407	12143	13686
V	168.6	167.4	200.5	192.2	199.2	197.9	172.4	199.4	190	155.2	164.2	180.2
Cr	396.8	371.2	229	283.3	299	294.4	266.2	313.3	285.6	291.4	315.6	260.5
Mn	1163	1157	1166	1157	1103	1077	1057	1120	1050	1124	1067	1101
Co	57.42	56.77	40.19	43.57	41.48	39.79	38.19	41.11	37.72	46.86	46.15	39.3
Ni	280.7	275.7	102.3	118.4	107.4	84.22	81.02	88.9	83.78	169.2	161.8	89.67
Cu	58.82	57.62	68.42	67.77	65.18	66.43	63.2	58.15	64.56	63.07	65.24	54.26
Zn	123.6	125.5	144	135.6	124.2	120.3	119.4	122	118.4	123.7	132.3	117.7
Ga	19.37	19.32	23.12	21.95	21.42	21.82	21.14	22.46	21.24	20.46	20.36	21.12
Ge	1.375	1.289	1.5	1.401	1.441	1.782	1.407	1.847	1.846	1.421	1.731	1.472
Rb	36.94	36.55	49.65	41.28	41.03	29.88	33.73	27.41	30.8	23.43	26.04	26.54
Sr	562.4	572.7	622.3	630.4	646.7	519.4	549.1	551.1	521.3	469.8	430.7	492.7
Y	19.54	19.39	25.17	22.75	21.9	20.21	21.39	20.84	19.73	19.32	17.86	21.12
Zr	168.6	167.2	231.6	193.3	188	201.6	167.9	203.5	199.2	131.9	155.7	152.7
Nb	39.61	38.73	52.06	45.04	43.42	33.64	32.23	33.43	32.47	25.02	24.86	28.59
Cs	0.468	0.462	0.669	0.464	0.635	0.229	0.508	0.449	0.342	0.381	0.396	0.449
Ba	454.8	445.5	572.2	517.7	499.9	425.5	410.2	423.8	414.2	288.9	284.5	329.1
La	28.96	28.3	37.53	33.19	31.81	25.13	24.89	25.69	24.35	18.55	18.86	22.2
Ce	58	56.81	74.06	65.78	64.14	50.37	50.34	51.41	50.26	38.38	37.81	46.05
Pr	6.93	6.832	8.931	7.96	7.728	6.388	6.498	6.364	6.155	4.783	4.706	5.587
Nd	28.21	27.49	36.05	32	31.22	26.95	25.95	27.54	26.32	20.1	20.62	23.22
Sm	6.36	6.302	8.027	7.298	7.166	6.715	6.339	6.813	6.473	5.135	5.328	5.834
Eu	2.134	2.11	2.598	2.432	2.395	2.244	2.19	2.273	2.187	1.843	1.813	2.002
Gd	5.997	6.053	7.674	7.005	6.903	6.272	6.28	6.471	6.278	5.322	5.502	5.899
Tb	0.861	0.875	1.088	1.02	0.975	0.902	0.92	0.937	0.869	0.803	0.752	0.879
Dy	4.44	4.394	5.53	5.155	5.027	4.697	4.741	4.833	4.644	4.291	4.194	4.63
Ho	0.767	0.752	0.97	0.898	0.881	0.821	0.838	0.842	0.823	0.754	0.751	0.825
Er	1.786	1.78	2.278	2.092	2.032	1.956	1.936	1.99	1.953	1.838	1.752	1.94
Tm	0.22	0.223	0.291	0.272	0.26	0.251	0.256	0.26	0.248	0.24	0.23	0.252
Yb	1.268	1.275	1.635	1.495	1.459	1.416	1.4	1.486	1.457	1.337	1.33	1.427
Lu	0.175	0.176	0.22	0.209	0.201	0.212	0.196	0.216	0.209	0.187	0.197	0.197
Hf	4.847	4.806	6.411	5.774	5.546	4.818	4.931	4.56	4.504	3.952	3.515	4.72
Ta	2.41	2.362	3.277	2.837	2.712	2.069	1.919	1.98	1.966	1.539	1.551	1.775
Pb	3.366	3.805	4.686	4.666	3.823	3.16	2.911	3.243	3.116	2.792	3.255	3.069
Th	4.471	4.391	5.972	5.187	5.051	4.189	3.695	3.902	3.796	2.684	2.825	3.396
U	0.959	0.929	1.264	1.146	1.032	0.932	0.859	0.914	0.902	0.67	0.752	0.766
Sample	DF2-1	DF2-2	DF2-3	DF3-1	DF3-2	DF3-3	DW-1	DW-2	DW-3	DWL-1	DWL-2	DWL-3
Sc	17.72	19.75	19.36	18.84	19.87	19.82	21.49	21.03	19.83	21.35	17.29	16.25
Ti	11446	11567	11254	11664	11598	12081	10611	10196	9600	10444	18914	19075
V	147.5	148.4	155.6	158.7	154.3	165.6	147.3	137.7	132.2	140.9	173.5	163.1
Cr	268.9	252.7	272.9	286.8	258.9	297.5	195.5	192.4	190.1	196.2	244.9	226.2

Mn	1076	1068	1008	1051	1082	1090	1155	1138	1122	1125	1254	1199
Co	40.63	43.34	40.73	43.85	42.27	43.3	44.85	44.58	42.91	44.98	49.64	47.49
Ni	148.2	159.2	145.7	163.9	153	159.3	114.1	111.6	111.7	117.4	137.7	131.9
Cu	57.33	64.78	62.83	65.66	66.55	69.02	71.61	70.81	70.34	71.81	81.03	74.21
Zn	110.2	119.5	111.1	116.4	119.1	118.6	116.8	117.8	109.9	125.3	153.5	152.3
Ga	19.42	19.57	19.91	20.86	20.03	20.98	19.79	19.82	19.17	19.88	22.81	22.59
Ge	1.646	1.481	1.69	1.741	1.541	1.805	1.502	1.471	1.443	1.508	1.456	1.338
Rb	19.53	17.29	19.21	18.91	17.43	19.06	8.878	8.458	6.188	8.758	39.35	38.97
Sr	349.9	342.7	319.2	332.2	348.8	334.2	261.5	259.9	263.9	266.3	686.3	686.3
Y	18.66	19.8	24.18	19.3	20.26	19.5	16.85	16.68	16.09	23.15	41.6	28.61
Zr	127.9	110.6	132.2	134.4	112.7	136.8	86.86	86.94	81.34	86.55	251	267
Nb	14.46	14.49	14.54	15.08	14.8	15.11	11	11.04	10.29	10.87	50.11	49.73
Cs	0.497	0.433	0.472	0.467	0.434	0.465	0.177	0.178	0.089	0.18	0.54	0.674
Ba	182.5	180.1	186.1	181.5	181.6	182.2	106.8	108.1	100.3	119.5	637.8	589.1
La	12.3	12.19	15.15	13.31	12.46	12.95	7.686	7.706	7.24	9.465	35.91	35.38
Ce	25.94	26.58	31.19	28.24	26.63	27.07	16.99	17.05	16.09	19.75	71.19	72.82
Pr	3.401	3.409	3.836	3.578	3.393	3.589	2.265	2.261	2.131	2.496	8.955	8.766
Nd	15.8	15.26	17.87	16.4	15.36	16.41	10.7	10.81	10.08	11.95	38.39	37.13
Sm	4.438	4.496	5.259	4.871	4.46	4.766	3.39	3.375	3.199	3.722	9.374	8.963
Eu	1.664	1.672	1.866	1.744	1.648	1.711	1.342	1.327	1.281	1.486	3.228	3.034
Gd	4.761	5.09	6.04	5.18	5.109	5.356	4.096	4.011	3.862	4.803	9.74	8.586
Tb	0.773	0.803	0.849	0.782	0.78	0.76	0.64	0.64	0.616	0.765	1.398	1.219
Dy	4.167	4.288	4.725	4.298	4.242	4.301	3.689	3.609	3.37	4.177	7.168	6.118
Ho	0.785	0.771	0.918	0.796	0.78	0.815	0.675	0.671	0.624	0.796	1.298	1.025
Er	1.833	1.911	2.21	1.964	1.866	1.924	1.662	1.655	1.555	1.983	2.931	2.324
Tm	0.235	0.251	0.285	0.257	0.242	0.251	0.22	0.221	0.207	0.252	0.347	0.279
Yb	1.41	1.438	1.668	1.475	1.392	1.498	1.273	1.245	1.169	1.394	1.831	1.519
Lu	0.202	0.2	0.232	0.217	0.198	0.222	0.18	0.179	0.163	0.204	0.248	0.199
Hf	3.149	3.678	3.28	3.362	3.626	3.316	2.959	2.88	2.687	2.958	6.561	6.316
Ta	0.942	0.911	0.908	0.917	0.937	0.885	0.769	0.692	0.624	0.694	3.126	3.003
Pb	1.781	1.98	2.438	2.528	2.09	1.944	0.981	0.945	0.66	1.123	2.408	2.944
Th	2.107	1.987	2.166	2.09	2.039	2.002	1.131	1.081	0.981	1.107	5.07	4.927
U	0.522	0.476	0.55	0.531	0.477	0.511	0.293	0.286	0.254	0.271	1.024	0.981

Sample	MX-1	MX-2	MX-3	BL-1	BL-2	BL-3	LQ-1	LQ-2	LQ-3	LL-1	WF-1	GR-1
Sc	20.52	20.65	20.07	19.78	20.64	20.3	19.52	20.14	18.95	20.62	21.19	9.812
Ti	9613	10174	9369	9976	9858	9973	9421	10028	9473	9522	10196	9913
V	146.1	138.8	145.6	144.6	135.4	148	148.5	140.8	145.4	132.5	141.4	94.12
Cr	228.7	200.1	212.6	200.5	189.9	214.6	248.9	228.8	246.6	196.3	196.3	160.3
Mn	1046	1146	1081	1059	1044	1058	1035	1070	1075	1063	1109	779
Co	43.36	43.52	41.98	43.79	42.82	43.47	43.04	42.63	41.83	43.31	45.13	31.69
Ni	104.7	106	102.9	106.7	104.1	108.1	134.9	128.5	128.2	104.5	103.2	92.06
Cu	60.52	63.78	57.67	63.84	49.68	65.3	54.58	58.26	59.8	49.41	65.2	47.86
Zn	111.5	115.9	112	113.3	115.3	112.2	107.2	110.6	116.3	111.1	115.9	171.2
Ga	19.91	19.24	19.12	19.85	19.33	19.18	18.92	19.07	18.54	19.28	19.83	28.69
Ge	1.825	1.456	1.745	1.82	1.426	1.845	1.874	1.457	1.843	1.498	1.42	1.267

(*continued on next page*)

Table 3 (*continued*)

Sample	MX-1	MX-2	MX-3	BL-1	BL-2	BL-3	LQ-1	LQ-2	LQ-3	LL-1	WF-1	GR-1
Rb	8.802	8.421	8.2	8.225	8.037	8.623	22.32	21.53	24.58	7.792	7.305	60.16
Sr	253.5	256.8	243.9	245.1	266.8	247.9	310.2	321.7	302.7	262.6	260.8	727.9
Y	16.14	17.1	16.63	18.85	25.6	15.28	16.21	17.93	16.11	15.85	25.51	14.81
Zr	97.2	87.59	97.53	96.49	82.18	97.52	117.1	101.6	118	81.08	84.17	405.8
Nb	9.549	10.19	9.903	9.874	9.937	10.17	16.45	16.64	16.12	9.629	9.552	73.58
Cs	0.151	0.143	0.141	0.153	0.133	0.152	0.513	0.511	0.552	0.116	0.108	0.647
Ba	110	111.6	122.2	128.2	115.1	112.7	237.7	231.8	229.1	114.5	115	623.9
La	8.108	7.849	8.053	11.5	9.236	7.555	14.32	15.11	14.52	7.27	8.875	44.34
Ce	18.6	17.63	17.25	25.43	19.27	16.52	28.41	29.28	28.5	16.23	18.87	82.95
Pr	2.33	2.348	2.253	3.237	2.375	2.21	3.487	3.609	3.455	2.152	2.292	9.423
Nd	11.15	11	11.03	15.21	11.38	10.85	15.3	15.13	15.12	10.2	10.95	35.16
Sm	3.587	3.516	3.461	4.525	3.568	3.437	4.014	3.961	3.917	3.186	3.502	7.579
Eu	1.352	1.361	1.317	1.708	1.455	1.321	1.443	1.425	1.417	1.27	1.372	2.504
Gd	4.045	4.093	3.977	4.968	4.643	3.896	4.232	4.319	4.22	3.699	4.574	6.47
Tb	0.627	0.655	0.598	0.724	0.73	0.595	0.619	0.689	0.636	0.598	0.72	0.863
Dy	3.547	3.679	3.32	4.118	4.202	3.291	3.485	3.764	3.44	3.362	4.051	3.774
Ho	0.653	0.674	0.642	0.748	0.824	0.625	0.662	0.696	0.652	0.61	0.808	0.543
Er	1.619	1.664	1.556	1.817	2.059	1.53	1.593	1.709	1.638	1.538	2.047	1.125
Tm	0.222	0.219	0.204	0.244	0.261	0.196	0.213	0.23	0.218	0.203	0.263	0.131
Yb	1.28	1.243	1.2	1.366	1.473	1.174	1.262	1.325	1.264	1.171	1.493	0.683
Lu	0.19	0.183	0.182	0.204	0.208	0.178	0.187	0.189	0.189	0.163	0.217	0.092
Hf	2.485	2.882	2.443	2.549	2.726	2.522	2.763	3.26	2.992	2.679	2.843	9.267
Ta	0.602	0.633	0.616	0.634	0.609	0.646	0.977	1.033	1.019	0.607	0.615	4.662
Pb	0.895	1.097	1.017	1.071	1.016	1.133	2.971	2.735	9.349	1.383	0.989	3.983
Th	1.117	1.117	1.195	1.096	1.053	1.18	2.95	2.813	2.935	1.052	1.049	7.84
U	0.299	0.251	0.321	0.263	0.241	0.291	0.635	0.587	0.645	0.238	0.282	1.613

Sample	GR-2	GR-3	MT-1	TJ-1	YN-1	ZW-1	ZW-2	BB-1	NX-1	BP-1	BP-2	BP-3
Sc	9.941	9.79	17.74	20.41	20.39	13.64	13.50	17.16	16.30	21.05	21.37	21.00
Ti	9793	9653	11062	9276	9392	12209	12311	11109	10684	12845	12851	12765
V	107.4	105.20	145.20	142.80	130.00	128.60	144.00	146.10	139.60	185.40	180.60	194.00
Cr	198	208.40	272.60	224.50	197.90	226.70	252.20	253.50	265.00	296.30	294.20	310.90
Mn	771	751	1069	1032	1105	949	959	1055	1028	1145	1173	1158
Co	31.49	32.33	46.69	43.87	43.57	39.59	42.83	45.32	44.54	50.06	50.84	50.96
Ni	92.08	92.23	160.30	107.40	104.30	107.80	116.80	131.40	143.50	214.00	212.50	214.00
Cu	48.36	48.62	65.87	55.31	48.97	55.97	60.02	65.12	61.70	65.22	64.10	65.40
Zn	143.5	145.30	126.40	110.70	109.70	145.10	135.40	127.60	118.90	113.70	110.70	114.60
Ga	29.36	28.91	20.84	18.95	19.10	25.34	25.63	22.37	21.58	19.19	18.93	19.63
Ge	1.483	1.47	1.78	1.74	1.41	1.31	1.60	1.71	1.67	1.39	1.43	1.76
Rb	65.33	64.23	25.40	7.67	7.23	44.52	48.85	29.53	28.21	27.87	27.15	29.32
Sr	700.1	700.10	429.90	242.00	253.00	698.40	684.60	492.80	487.30	510.50	514.40	496.30
Y	13.81	14.31	16.51	29.45	15.73	16.37	14.93	15.63	15.19	19.17	19.03	18.39
Zr	402.2	396.60	147.20	94.00	78.26	289.00	282.10	175.30	150.50	134.20	132.30	160.70
Nb	74.48	74.61	30.89	9.08	9.11	55.94	54.27	34.31	33.08	31.66	31.09	32.30

Cs	0.497	0.72	0.32	0.14	0.11	0.60	0.70	0.22	0.13	0.35	0.30	0.17
Ba	669.7	633.80	331.90	103.60	109.10	544.80	523.60	409.30	406.20	345.20	340.60	358.30
La	45.25	44.61	20.33	10.79	6.99	34.68	34.59	22.74	21.79	21.16	21.05	21.77
Ce	86.51	84.52	38.70	21.30	15.59	67.24	65.75	43.76	42.49	43.20	42.45	43.03
Pr	9.823	9.48	4.65	2.44	2.05	7.71	7.62	5.30	4.99	5.19	5.13	5.25
Nd	37.58	37.62	19.61	12.08	9.93	30.26	31.04	22.18	21.11	21.21	21.17	22.40
Sm	8.126	8.19	5.18	3.78	3.13	6.77	7.07	5.48	5.34	5.11	5.07	5.51
Eu	2.629	2.60	1.79	1.48	1.26	2.28	2.31	1.96	1.88	1.80	1.75	1.87
Gd	6.673	6.86	5.05	5.02	3.76	5.94	6.17	5.25	5.16	5.11	5.11	5.40
Tb	0.855	0.86	0.71	0.74	0.59	0.84	0.80	0.75	0.73	0.77	0.77	0.75
Dy	3.789	3.72	3.76	4.29	3.34	3.93	3.81	3.77	3.60	4.10	4.09	4.03
Ho	0.567	0.57	0.67	0.92	0.63	0.62	0.62	0.64	0.62	0.71	0.71	0.74
Er	1.11	1.12	1.54	2.25	1.56	1.37	1.33	1.49	1.42	1.78	1.77	1.73
Tm	0.125	0.12	0.19	0.29	0.21	0.16	0.16	0.18	0.18	0.23	0.23	0.23
Yb	0.711	0.69	1.09	1.61	1.23	0.87	0.92	1.05	1.02	1.31	1.34	1.41
Lu	0.1	0.10	0.16	0.25	0.17	0.12	0.12	0.16	0.15	0.18	0.19	0.20
Hf	8.912	8.86	3.37	2.47	2.71	6.71	5.99	4.03	3.84	3.88	3.92	3.66
Ta	4.993	4.87	1.78	0.56	0.57	3.38	3.39	2.11	2.09	1.94	1.93	2.00
Pb	4.26	4.00	1.51	1.03	0.83	2.93	2.54	2.79	1.63	2.34	2.29	2.36
Th	8.824	8.65	3.47	1.05	1.02	5.42	5.39	3.66	3.64	3.20	3.23	3.38
U	1.567	1.84	0.76	0.28	0.23	1.30	1.26	0.72	0.56	0.76	0.67	0.73

Sample	BP-4	BP-5	LQZ-1	LQZ-2	LQZ-3	JZ-1	JZ-2	ZT-1	ZT-2	ZT-3	HQ-1	HQ-2
Sc	20.75	21.94	19.97	20.61	19.62	19.84	21.09	20.24	20.55	19.77	18.75	19.16
Ti	12203	12911	9447	10055	9689	12256	12587	11125	11619	11232	10661	10520
V	191.10	196.80	147.5	139.3	136.3	158.7	171.7	168.3	157	164.1	132.2	132.8
Cr	308.20	326.50	254.9	224.8	224.9	246.1	269.3	284	265.7	295.6	217.9	211.4
Mn	1109	1206	1086	1139	1092	1021	1189	1142	1179	1138	1011	1059
Co	50.10	52.36	43.63	45.86	43.49	46.63	53.1	46.84	49.3	48.38	42.46	42.68
Ni	212.10	219.60	132.8	140.1	133.9	144.8	169.2	200.5	201.2	191.6	125.2	125
Cu	60.11	64.16	58.74	59.86	59.59	57.95	60.17	59.86	63.69	68.26	56.52	59.31
Zn	111.40	114.80	107.4	118.6	111	118.8	130	114.8	120.7	116.2	112.5	113.1
Ga	19.31	19.89	19.4	19.53	19	19.52	20.07	19.59	19.47	20.2	19.09	19.32
Ge	1.71	1.75	1.871	1.502	1.462	1.412	1.473	1.799	1.431	1.781	1.368	1.432
Rb	30.98	29.96	20.86	19.08	19.37	20.86	22.06	20.96	21.24	23.02	8.094	7.708
Sr	476.50	504.20	304.7	318.5	314.1	413.1	426.5	346.9	369.4	351.6	334.9	338.6
Y	17.36	17.65	15.96	17.88	17.22	19.17	19.58	18.01	18.92	17.74	15.93	16.92
Zr	157.40	157.10	113.8	98.06	96.22	122.3	126.2	135.4	116.1	135.4	96.07	101
Nb	30.33	31.37	13.81	14.26	14.07	22.85	23.36	19.8	19.46	19.39	13.69	13.91
Cs	0.37	0.36	0.474	0.446	0.453	0.321	0.352	0.452	0.465	0.476	0.15	0.161
Ba	344.30	346.20	194.4	195.9	192	251.5	254.5	227.8	228	230.4	163.7	177.3
La	21.17	21.51	12.47	13.06	12.4	16.57	16.89	16.03	15.82	16.04	10.56	11.41
Ce	41.86	42.03	25.82	26.87	25.76	34.24	35.14	32.6	32.82	32.58	22.73	24.49
Pr	5.05	5.08	3.157	3.315	3.162	4.208	4.308	4.085	4.023	3.981	2.861	3.075
Nd	22.04	22.01	14.04	13.95	13.51	17.86	18.18	17.39	16.72	17.34	12.64	13.53
Sm	5.35	5.38	3.798	3.77	3.612	4.631	4.736	4.679	4.323	4.578	3.562	3.817

(*continued on next page*)

Table 3 (*continued*)

Sample	BP-4	BP-5	LQZ-1	LQZ-2	LQZ-3	JZ-1	JZ-2	ZT-1	ZT-2	ZT-3	HQ-1	HQ-2
Eu	1.83	1.86	1.37	1.406	1.328	1.648	1.715	1.599	1.566	1.592	1.402	1.443
Gd	5.21	5.15	4.183	4.259	4.074	4.857	5.159	4.825	4.768	4.816	4.011	4.271
Tb	0.72	0.76	0.629	0.666	0.638	0.75	0.788	0.708	0.734	0.703	0.607	0.658
Dy	4.03	3.95	3.458	3.727	3.546	4.054	4.23	3.996	3.999	3.906	3.395	3.592
Ho	0.74	0.73	0.67	0.685	0.658	0.741	0.775	0.715	0.751	0.71	0.619	0.662
Er	1.70	1.76	1.592	1.714	1.645	1.821	1.84	1.745	1.8	1.792	1.506	1.645
Tm	0.23	0.24	0.219	0.229	0.219	0.23	0.248	0.237	0.235	0.234	0.195	0.211
Yb	1.35	1.30	1.279	1.344	1.245	1.319	1.392	1.321	1.379	1.387	1.14	1.231
Lu	0.20	0.20	0.192	0.191	0.181	0.19	0.203	0.199	0.195	0.202	0.158	0.179
Hf	3.57	3.56	2.737	3.116	2.981	3.635	3.817	3.126	3.542	3.255	2.965	3.17
Ta	1.95	1.94	0.849	0.923	0.865	1.377	1.414	1.227	1.205	1.235	0.827	0.88
Pb	2.22	2.25	2.324	2.829	4.565	1.799	1.954	2.521	2.859	2.478	3.123	1.878
Th	3.26	3.19	2.282	2.316	2.259	2.472	2.623	2.87	2.603	2.801	1.6	1.827
U	0.81	0.79	0.529	0.516	0.494	0.578	0.642	0.665	0.585	0.666	0.359	0.398

Sample	HQ-3	YL-1	YL-2	SMP-1	SMP-2	SMP-3	SMP-4	SMP-5	NL-1	NL-2	NL-3	PL-1
Sc	19.3	19.65	18.63	18.68	18.68	22.62	21.86	21.87	19.7	19.73	19.98	18.88
Ti	10850	10660	10378	10662	10491	12034	11087	11672	11332	11241	11289	9942
V	150.1	144.4	149.3	133.5	142.5	170	168.5	159.8	149.5	145.7	158.9	129
Cr	243.3	224.7	240.4	200.3	204	307.3	299.7	248.3	225.8	242.8	265.2	426
Mn	1057	1039	1050	1191	1212	1230	1174	1191	1160	1093	1109	1061
Co	44.69	43.58	42.09	40.77	41.44	51.8	45.8	47.4	44.13	41.85	43.87	50.36
Ni	129.7	131.1	128.1	112.9	113.1	168.3	144.2	153.3	177	154.7	167.4	268.8
Cu	55.11	43.36	64.36	51.66	51.36	65.48	59.62	61.81	65.6	88.26	69.4	58.02
Zn	115.7	118.8	113.9	113.4	112.6	126.9	115.7	125.8	111.3	111.3	111.3	104.7
Ga	20.64	19.57	19.06	19.24	19.32	20.46	20.51	19.98	18.88	19.12	19.45	17.82
Ge	1.805	1.405	1.791	1.44	1.413	1.925	1.757	1.458	1.401	1.401	1.735	1.347
Rb	10.19	9.071	11.52	15.82	15.59	15.38	14.94	13.5	15.51	15.24	26.91	19.91
Sr	323.3	346.9	331	353.9	352.1	316.7	313.5	318.9	401.4	363.4	403.8	403.3
Y	16.3	17.29	15.88	17.33	17.33	18.19	18.98	19.77	19.63	19.76	19.68	15.98
Zr	123.3	106.1	121.9	108.9	109.4	122.2	116.2	102.6	116.4	105.1	144.3	95.78
Nb	14.61	14.76	14.74	16.22	16.12	15.33	14.63	15.3	29.53	21.53	31.41	20.75
Cs	0.229	0.193	0.233	0.207	0.21	0.239	0.224	0.186	0.163	0.194	0.244	0.174
Ba	177.3	183.5	189	200.5	198	176.7	170.7	173.3	318.4	251.8	337.3	255.7
La	11.78	12.18	12.39	13.02	12.95	11.51	10.88	11.04	21.51	15.92	24.41	15.46
Ce	24.54	26.17	25.21	27.87	27.69	24.9	22.79	23.52	41.58	32.05	45.5	31.04
Pr	3.165	3.299	3.245	3.486	3.433	3.169	2.984	3.007	4.799	3.801	5.373	3.646
Nd	14.56	14.32	14.78	15.23	15.18	14.57	14.14	13.54	19.29	15.99	22.06	15.12
Sm	4.17	4.003	4.178	4.119	4.108	4.457	4.232	4.053	4.663	4.343	5.45	3.832
Eu	1.514	1.492	1.502	1.524	1.495	1.581	1.634	1.506	1.688	1.579	1.795	1.446
Gd	4.418	4.409	4.357	4.538	4.465	4.838	4.7	4.742	4.968	4.871	5.452	4.129
Tb	0.658	0.682	0.647	0.689	0.698	0.731	0.691	0.745	0.781	0.751	0.801	0.636
Dy	3.695	3.709	3.53	3.716	3.741	4.142	3.902	4.191	4.143	4.109	4.341	3.477
Ho	0.663	0.688	0.673	0.69	0.689	0.776	0.736	0.77	0.751	0.757	0.783	0.64

Er	1.637	1.669	1.63	1.705	1.653	1.89	1.824	1.897	1.831	1.871	1.908	1.576
Tm	0.216	0.221	0.213	0.222	0.221	0.249	0.237	0.256	0.244	0.245	0.259	0.207
Yb	1.245	1.263	1.251	1.264	1.284	1.481	1.419	1.477	1.371	1.424	1.477	1.167
Lu	0.186	0.182	0.189	0.18	0.176	0.223	0.211	0.203	0.196	0.193	0.219	0.163
Hf	3.028	3.403	3.074	3.612	3.495	3.095	2.938	3.349	3.506	3.302	3.474	3.026
Ta	0.903	0.94	0.921	0.994	1.001	0.926	0.911	0.911	1.673	1.254	1.887	1.245
Pb	2.445	2.099	1.973	2.292	2.236	6.328	1.319	2.389	2.018	1.775	2.075	1.923
Th	1.799	2.023	2.046	2.029	2.007	1.607	1.612	1.561	3.265	2.435	3.885	2.406
U	0.423	0.384	0.476	0.437	0.441	0.405	0.393	0.372	0.664	0.5	0.826	0.503

Sample	PL-2	PL-10	DL-1	DL-2	LH-1	LH-2	LH-3	LH-4	LM-1	LM-2
Sc	20.25	19.5	18.63	18.42	19.11	18.86	18.78	19.61	18.06	19.51
Ti	13134	10316	12318	12020	13784	13995	12929	14001	11240	12108
V	153	130.1	150.5	145.4	166.4	178.8	158.4	165.4	161.2	156
Cr	287.8	559.1	262.3	265.7	219.9	238.5	268.2	263.7	292.3	292.2
Mn	1105	1158	1165	1205	1102	1091	1099	1128	1423	1481
Co	45.83	57.55	49.26	48	39.01	38.44	43.08	42.89	50.06	52.96
Ni	192.2	383.7	172.9	169.8	87.73	88.56	131.7	122.7	182.1	199.4
Cu	69.84	56.95	57.41	60.04	56.88	58.67	58.83	64.12	62.58	63.13
Zn	116.5	104.8	122	124.2	119.3	119.2	119.1	123.5	113.2	123.3
Ga	19.54	16.79	20.06	19.73	21.14	21.94	20.43	21.12	19.22	19.34
Ge	1.453	1.264	1.464	1.406	1.447	1.807	1.454	1.404	1.677	1.404
Rb	23.52	21.28	27.58	27	26.41	29.29	25.36	27.32	27.01	24.7
Sr	381.7	413.5	429.9	411.5	525.6	501	512.2	520	405	451.2
Y	18.91	15.45	19.64	19.51	22.53	19.94	20.86	21.46	17.33	18.77
Zr	120.4	107.2	133.5	132.1	152.2	180.7	143.1	149.2	149.4	130.4
Nb	25.09	28.69	24.41	24.19	28.77	28.2	26.31	27.44	24.17	24.42
Cs	0.122	0.133	0.517	0.463	0.476	0.52	0.433	0.474	0.509	0.433
Ba	297.3	293.1	281.1	269	302.7	306.8	291.1	296.8	272.7	282.3
La	17.36	20.49	18.84	18.33	21.61	21.23	20.36	20.74	18.68	18.26
Ce	34.5	39.9	39.25	38.39	44.3	43.25	41.24	43.09	36.45	37.73
Pr	4.13	4.62	4.77	4.622	5.496	5.475	5.068	5.257	4.476	4.591
Nd	17.6	18.34	19.88	19.25	22.94	23.62	21.31	22.2	19.72	19.27
Sm	4.629	4.197	5.091	4.912	5.805	6.038	5.315	5.483	5.066	4.905
Eu	1.671	1.503	1.736	1.687	2.023	2.031	1.844	1.921	1.719	1.705
Gd	5.043	4.322	5.31	5.245	6.036	5.972	5.608	5.825	5.034	5.02
Tb	0.756	0.64	0.805	0.782	0.894	0.85	0.829	0.87	0.726	0.776
Dy	4.125	3.417	4.221	4.132	4.808	4.573	4.316	4.589	3.841	4.058
Ho	0.747	0.63	0.77	0.738	0.86	0.817	0.78	0.805	0.68	0.734
Er	1.817	1.504	1.827	1.805	2.06	1.909	1.852	1.992	1.662	1.758
Tm	0.243	0.194	0.244	0.23	0.265	0.26	0.245	0.247	0.213	0.226
Yb	1.312	1.102	1.359	1.287	1.527	1.5	1.376	1.467	1.217	1.335
Lu	0.185	0.163	0.189	0.183	0.21	0.212	0.201	0.203	0.184	0.182
Hf	3.952	3.242	4.101	4.144	4.461	4.202	4.214	4.535	3.486	3.972
Ta	1.573	1.842	1.494	1.506	1.789	1.795	1.59	1.721	1.517	1.526
Pb	1.614	2.101	2.861	3.118	2.885	3.063	3.41	3.284	2.691	3.162
Th	2.797	3.037	3.373	3.45	3.179	3.284	3.09	3.339	3.187	3.031
U	0.607	0.636	0.708	0.719	0.776	0.86	0.76	0.809	0.894	0.796

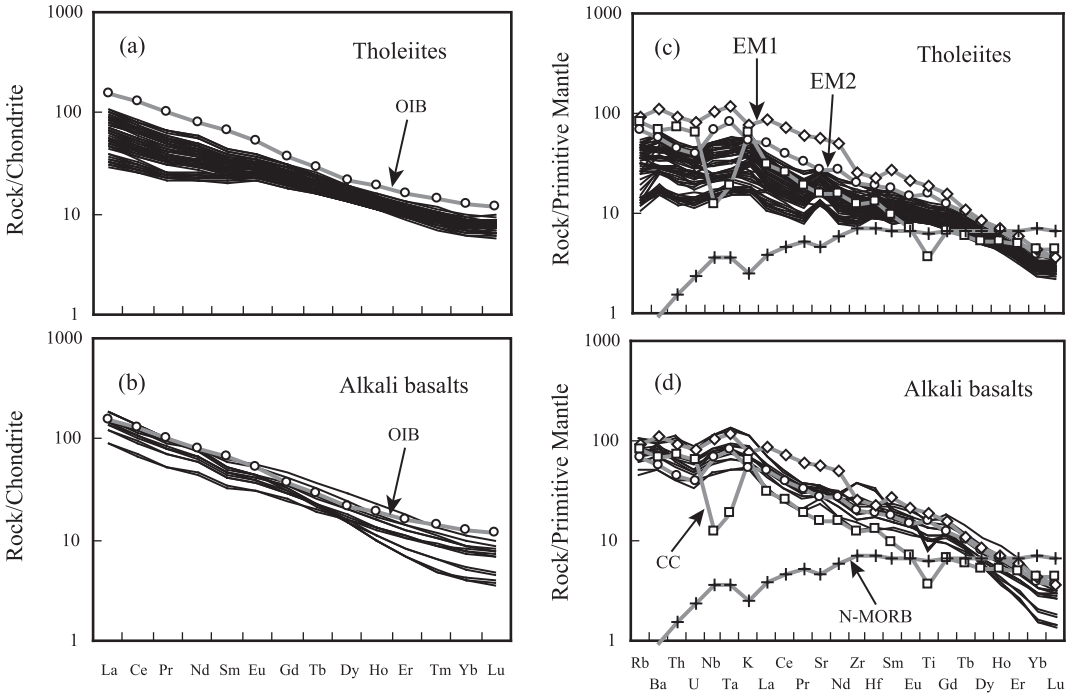

Fig. 6. (a, b) Chondrite-normalized REE patterns for Hainan tholeiites and alkali basalts, respectively. OIB is also plotted for comparison. Data sources of OIB and Chondrite is from Sun and McDonough (1989). (c, d) Primitive mantle-normalized incompatible trace element patterns for tholeiites and alkali basalts respectively. EM1, EM2, Continental Crust (CC for abbreviation), and N-MORB are also plotted for comparison. Data sources of EM1 (average of Tristan da Cunha) and EM2 (average of Samoa) is from Chauvel et al. (1997), Kogiso et al. (1997) and Willbold and Stracke (2006). Continental Crust is from Rudnick and Gao (2003), N-MORB is from Sun and McDonough (1989), and Primitive mantle is from McDonough and Sun (1995).

5. DISCUSSION

The composition of lava, as the final product of volcanism, is controlled by many factors, including the lithology and origin of the mantle source, mantle temperature and pressure, partial melting degrees (F), effects of post-magmatic modification, fractional crystallization and crustal contamination. Next we will explore the importance of these parameters and processes in the generation of the Hainan basalts.

5.1. Effects of post-magmatic alteration on the Hainan basalts

Petrographic observations and compositional variations of the whole rocks are combined to evaluate post-magmatic alteration and fractional crystallization of the Hainan basalts. Inspection of the samples under a microscope suggests that the samples are not obviously affected by alteration. Any post-magmatic alteration is limited to some early-stage (Miocene–Pliocene) tholeiites, in which the olivine phenocrysts have been partially altered to iddingsite. The range of LOI of the Hainan basalts is −0.0007 wt% to 0.0198 wt% with an average value of −0.0087 wt%, indicating that the Hainan basalts are hardly influenced by post-magmatic alteration. The good correlation between immobile incompatible elements, such as Zr, and potentially mobile incompatible elements, such as Rb, Ba, Th, U, La, Sr, (Fig. 7), further demonstrates that post-magmatic alteration is insignificant in the Hainan basalts. Some of the alkali basalts have lower Sr and Ba contents, consistent with the fractionation of plagioclase.

5.2. The role of fractional crystallization

Among the tholeiites, SiO_2 and Al_2O_3 contents increase sharply and the Ni abundances decrease sharply with falling MgO (Fig. 5a, c, i), suggesting the fractional crystallization of olivine. However, CaO and Sc contents correlate weakly negatively with MgO (Fig. 5e, j), and FeO^T and CaO/Al_2O_3 remain nearly constant with falling MgO (Fig. 5d, f), indicating that clinopyroxene and plagioclase are not the predominant phases in the fractionating mineral assemblages. Because Sc and Ca are compatible in clinopyroxene, and Ca and Al are compatible in plagioclase, if these phases were fractionating, CaO, Sc and CaO/Al_2O_3 would decease with falling MgO. On the other hand, in the alkali basalts, Ni contents correlate positively with MgO (Fig. 5i), whereas SiO_2, TiO_2, Al_2O_3, CaO, Na_2O, K_2O and Sc contents correlate negatively with MgO (Fig. 5a, b, c, e, g, h, j), and FeO^T and CaO/Al_2O_3 remain constant with decreasing MgO (Fig. 5d, f) when MgO >7.5 wt%. All of these features indicate that the alkali basalts only experienced olivine fractionation at MgO >7.5 wt%. However, TiO_2, FeO^T, CaO, Sc and CaO/Al_2O_3 decrease sharply with decreasing MgO at MgO <7.5 wt% (Fig. 5b, d, e, f, j).

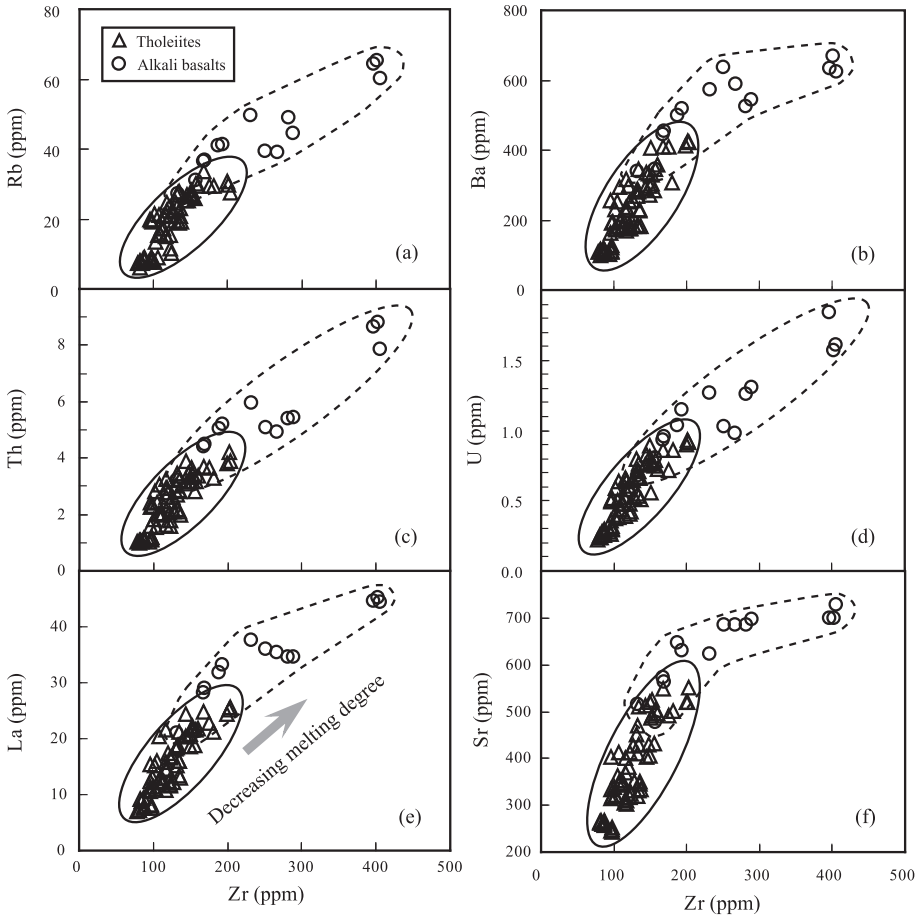

Fig. 7. Variation of Rb, Ba, Th, U, La and Sr versus Zr for the Hainan basalts. The solid and dashed lines define the range of tholeiites and alkali basalts respectively. As a whole, Rb, Ba, Th, U, La and Sr correlate positively with Zr, which demonstrates that post-magmatic alteration is insignificant in the Hainan basalts. Tholeiites have lower incompatible trace element concentrations than alkali basalts, indicating that the tholeiites were derived from higher degrees of melting than alkali basalts.

The SiO_2 contents correlate negatively with MgO but the gradient is steeper when MgO <7.5 wt% (Fig. 5a), and the Ni contents also correlate positively with MgO, yet the gradient becomes more gentle at MgO <7.5 wt% (Fig. 5i). These trends suggest that clinopyroxene or plagioclase, or even Fe–Ti oxide minerals started to fractionate from the alkali basalt magma at MgO <7.5 wt%. Meanwhile the Na_2O and K_2O contents correlate positively with MgO for the alkali basalts, suggesting that alkali-feldspar is not a crystallizing phase.

Furthermore, we have quantitatively modelled the crystal fractionation of Hainan basalts by the software PETROLOG 3 (Danyushevsky and Plechov, 2011), and the results are shown in Fig. 9. The samples PL-10 and YX-1 have the highest MgO contents and were chosen as the starting melt compositions for tholeiitic and alkalic series respectively. Olivine and clinopyroxene are used as potential crystallizing phases, because they are the major phenocrysts in the Hainan basalts. Olivine–melt equilibrium models are from Gaetani and Watson (2002), and clinopyroxene–melt equilibrium models are from Danyushevsky (2001). The default value 100% is assigned to the extent of fractionation for each mineral, corresponding to the case of pure fractional crystallization. QFM is set as the "Initial oxidation state". We modelled the crystal fractionation in 1 kbar and 3 kbar initial P for PL-10, and 1 kbar and 5 kbar initial P for YX-1. The value 0 wt% H_2O (dry), 1 wt%, and 2 wt% were respectively set in the starting compositions. From Fig. 9, we realize that, though with some scatter, modelled crystal fractionation of PL-10 under 3 kbar with no H_2O can approximately match the tholeiites. And modelled crystal fractionation of YX-1 under 5 kbar with no H_2O can approximately match the alkali basalts. Several alkaline samples (GR-1, 2, 3) having the lowest MgO and FeO^* deviate from the modelled fractional trend line, which may be due to the fractionation of Fe–Ti oxide minerals. This quantitative calculation further demonstrates our conclusion that all tholeiites and alkali basalts with MgO >7.5 wt% only experienced olivine fractionation.

Based on the systematic decrease of MgO, $\sum$FeO and TiO_2 with increasing SiO_2 in the Cenozoic basalts from Hainan Island, Ho et al. (2000) conclude that olivine,

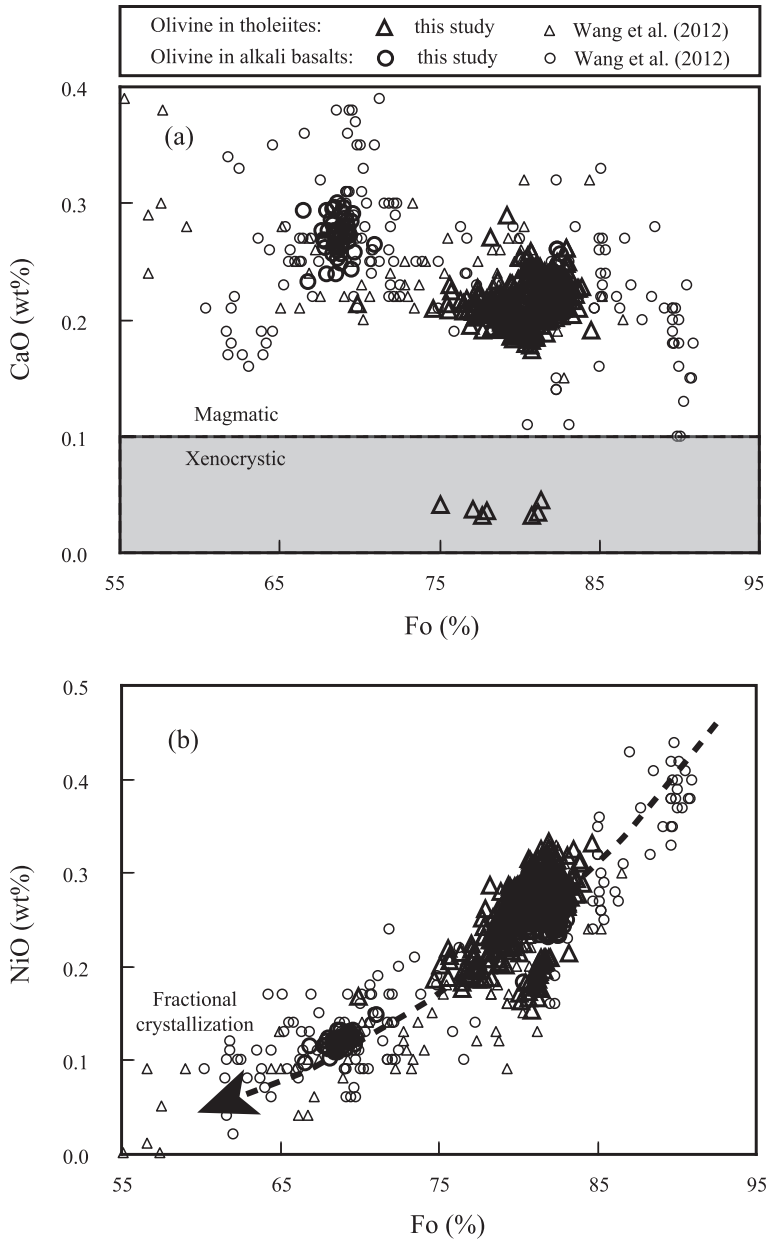

Fig. 8. (a) CaO and (b) NiO contents versus Fo of olivines in the Hainan basalts. Note that almost all olivines have CaO >0.1 wt%, and the NiO trend follows that of the fractional crystallization (see text for further explanation), indicating that the analyzed olivines crystallized from the magma rather than being mantle-derived xenocrysts.

clinopyroxene and Ti-bearing opaques may have fractionated from the magma system. Also Wang et al. (2012) suggest that the clinopyroxene fractionation has little effect on most of the tholeiites and alkali basalts with high Mg# (>61). Furthermore, petrographical observations demonstrate that only olivine phenocrysts are abundant in the tholeiites, whereas in the alkali basalts, not only is olivine abundant, but there are also numerous clinopyroxene (~7%) and plagioclase (5–7%) phenocrysts, and Fe–Ti oxides in the groundmass, which is consistent with observations from previous research (Ho et al., 2000; Wang et al., 2012).

5.3. Crustal contamination

In contrast to oceanic basalts, continental intra-plate basalts pass through thick continental crust prior to eruption and thus have a greater opportunity to become contaminated by the crust. Several lines of evidence suggest that crustal contamination was insignificant in the petrogenesis of the Hainan basalts. First, abundant mantle xenoliths and xenocrysts occur in the Hainan basalts (Fan and Hooper, 1989; Xu et al., 2003), indicating that the host magma ascended rapidly. In addition, the Hainan basalts display positive Nb and Ta anomalies in the primitive

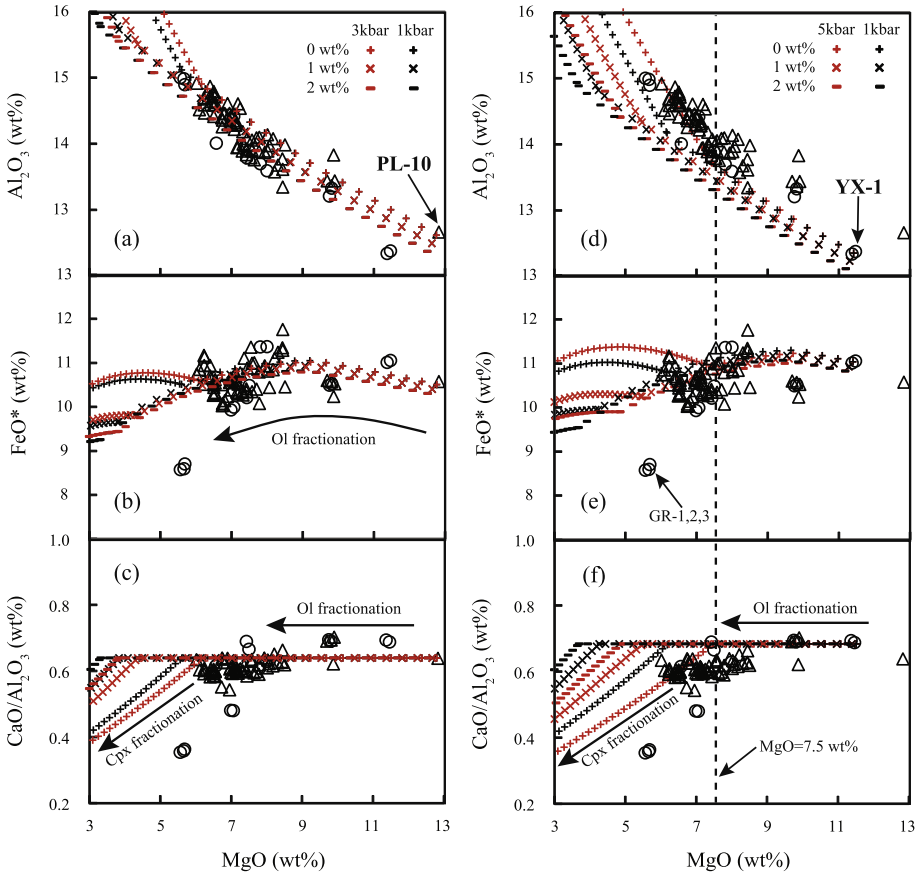

Fig. 9. Representative major elements (Al_2O_3, FeO^*) and major element ratios (CaO/Al_2O_3) plotted versus MgO for Hainan basalts and fractional crystallization paths modelled by the POTROLOG 3 program for the conditions indicated in (a and d) (see text for further explanation).

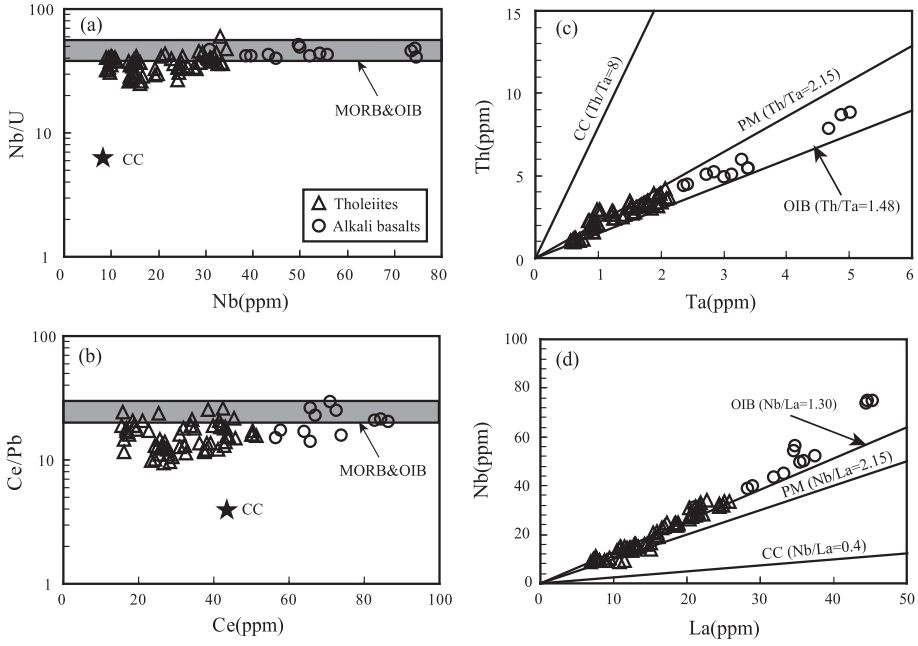

Fig. 10. (a) Nb/U versus Nb, (b) Ce/Pb versus Ce, (c) Th versus Ta, (d) Nb versus La for the Hainan basalts compared to MORB & OIB (Hofmann et al., 1986), Continental Crust (Rudnick and Gao, 2003), and Primitive mantle (McDonough and Sun, 1995).

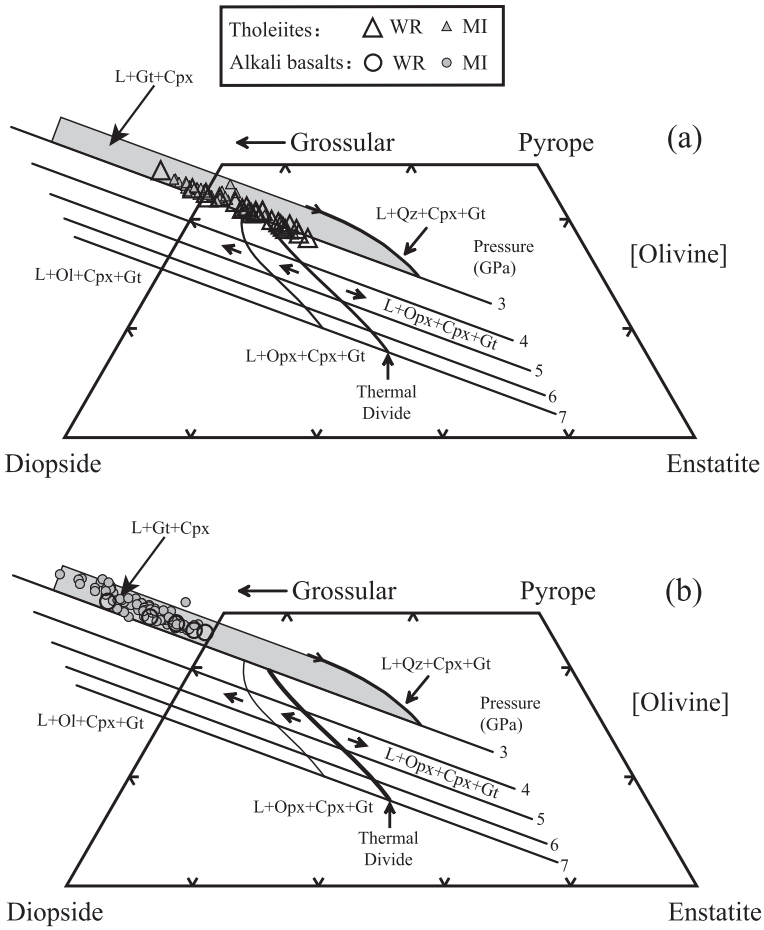

Fig. 11. (a, b) CS-MS-A diagram (Herzberg, 2011) of Hainan basalt whole rocks and melt inclusions that only experienced olivine fractionation (MgO >7.5 wt%). WR and MI denote whole rock and melt inclusions respectively as in Fig. 4. Abbreviations: L – liquid, Ol – olivine, Qz – quartz, Cpx – clinopyroxene, Opx – orthopyroxene, Gt – garnet. For tholeiites, all the melt inclusions and whole rocks plot in the field between L + Cpx + Gt and L + Cpx + Opx + Gt at ~3.0 GPa, but for alkali basalts, all the melt inclusions and whole rocks plot in the field of L + Cpx + Gt (see text for further explanation).

mantle-normalized incompatible elements spidergrams (Fig. 6c, d), further suggesting negligible contamination from the continental crust. Furthermore, oceanic basalts (MORB and OIB) have average Nb/U and Ce/Pb of 47 ± 7 and 25 ± 5, respectively (Hofmann et al., 1986), higher than that of continental crust (3.91 and 6.15, respectively (Rudnick and Gao, 2003)). In comparison, Nb/U and Ce/Pb in the Hainan basalts range from 25.9 to 59.6, with an average value of 37.4 ± 13, and 9.5–29.6, with an average value of 16.5 ± 9, respectively (Fig. 10a, b). These ratios are close to the average values for MORB and OIB, and higher than that of continental crust. Th/Ta (1.47–3.02) and Nb/La (0.84–1.67) in the Hainan basalts fall between primitive mantle and OIB (Fig. 10c, d), also indicating that the Hainan basalts did not suffer significant continental contamination. Lastly, Zou and Fan (2010) show that the Hainan basalts have strong ^{230}Th excesses, which cannot be produced by crustal contamination, because assimilation of crustal rocks ($^{230}Th/^{238}U = 1.0$) would reduce the extent of ^{230}Th excesses.

5.4. Probe into the mantle source of the Hainan basalts

5.4.1. Residual mineralogy and melting conditions of mantle source

During partial melting, the residual mineralogy of the magma source is one of the most significant factors influencing the compositions of basaltic magmas. Combining petrographical observations with MgO variation diagrams, the only phase to fractionate from alkali basalts with MgO >7.5 wt% and all the tholeiites was olivine. Thus, only samples with MgO >7.5 wt% were plotted on a CS-MS-A projection (Herzberg, 2011) to minimize the effect of clinopyroxene fractionation. In addition, melt inclusions with MgO >7.5 wt% are also plotted. As illustrated in Fig. 11, the fields defined by melt inclusions are consistent with those of the whole rocks, but the melt inclusions exhibit a wider range. For tholeiites, all the melt inclusions and whole rocks plot between L + Cpx + Gt and L + Cpx + Opx + Gt at ~3.0 GPa. This suggests that the residual minerals after melt extraction in the source of tho-

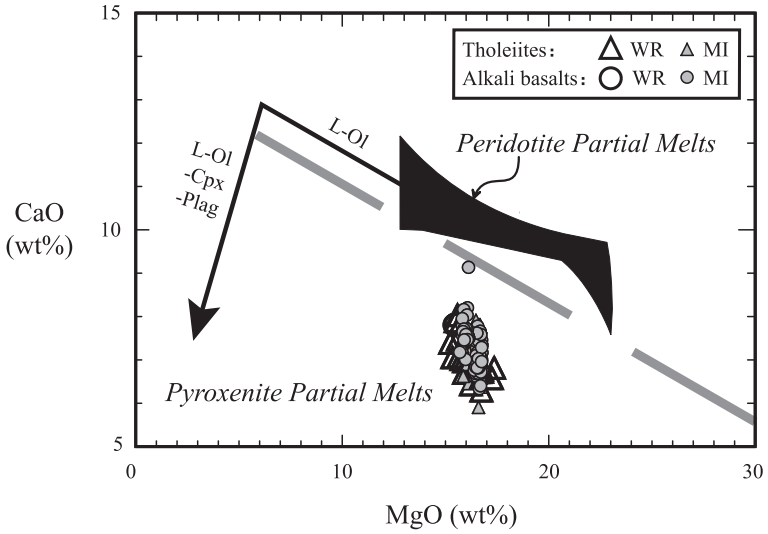

Fig. 12. CaO versus MgO of Hainan basalt primary magmas. Whole rocks and melt inclusions that experienced only olivine fractionation (>7.5 wt%) are corrected to be in equilibrium with an olivine composition of $Fo_{90.7}$ (most magnesian olivine found in the Hainan basalts, Wang et al. (2012)) by adding 0.1% equilibrium olivine (assuming that 10% of the total iron is Fe^{3+}, and assuming a constant $(Fe^{2+}/Mg)_{olivine}/(Fe^{2+}/Mg)_{melt} = 0.3$; Roeder and Emslie, 1970). The gray dotted line separating pyroxenite melts from peridotite melts is from Herzberg and Asimow (2008). Abbreviations are the same as in Fig. 10. Compared to peridotite melts, the primary magma compositions of Hainan whole rocks and melt inclusions have lower CaO, indicating the involvement of pyroxenite in their mantle source.

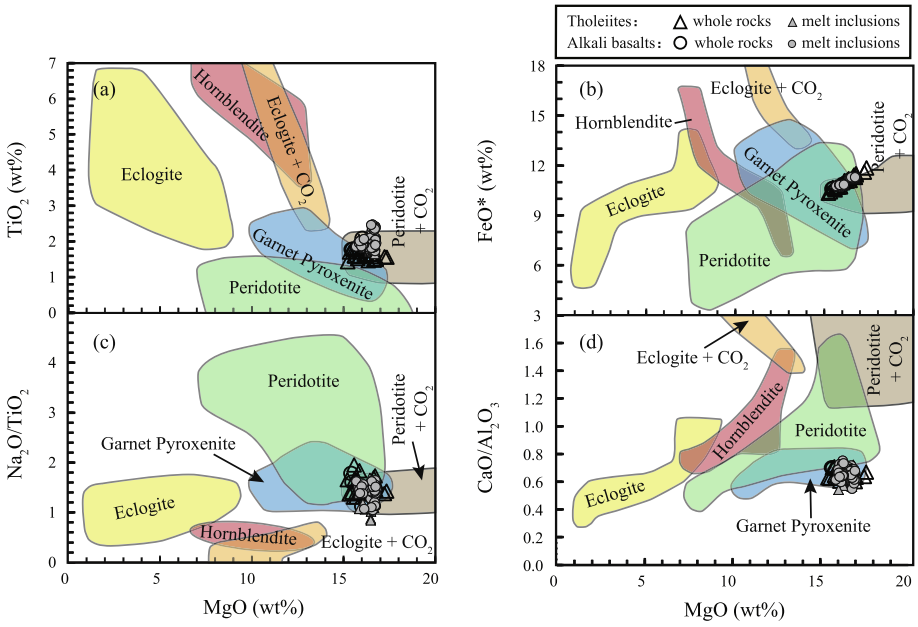

Fig. 13. Comparisons of major elements TiO_2 and FeO^* (a, b) and major element ratios Na_2O/TiO_2 and CaO/Al_2O_3 (c, d) between Hainan basalt primary magmas and high-pressure experimental partial melts of volatile-free peridotite (Hirose and Kushiro, 1993; Schwab and Johnston, 2001; Wasylenki et al., 2003; Laporte et al., 2004), peridotite + CO_2 (Dasgupta et al., 2007), eclogite (Pertermann and Hirschmann, 2003; Kogiso and Hirschmann, 2006), eclogite + CO_2 (Dasgupta et al., 2006), hornblendite (Pilet et al., 2008) and garnet pyroxenite (Hirschmann et al., 2003; Keshav et al., 2004).

leiites should be mainly Cpx and Gt, possibly Opx, but not Ol, and the melting pressure is possibly ~3.0 GPa. As for the alkali basalts, all the melt inclusions and whole rocks plot in the field of L + Cpx + Gt, indicating that their residual minerals are Cpx and Gt, but the melting pressure is hard to estimate (Herzberg, 2011).

Based on the correlations between the incompatible element ratios and the concentrations of Th adjusted to be in equilibrium with $Fo_{90.7}$ (most magnesian olivine) of the Hainan basalts, Wang et al. (2012) stated that the residual minerals for tholeiites were mainly olivine with the involvement of garnet and possibly amphibole, whereas

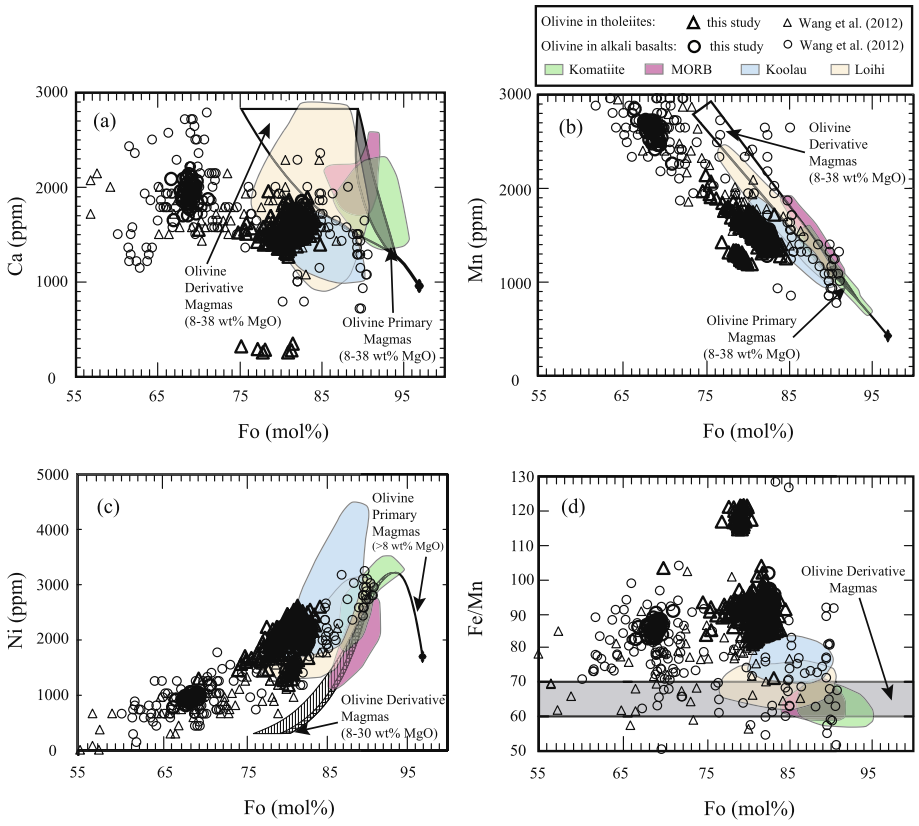

Fig. 14. (a) Ca, (b) Mn, (c) Ni and (d) Fe/Mn against Fo in olivine phenocrysts from the Hainan basalts, with reference to Herzberg (2011). The olivines from Komatiites, MORB, Koolau and Loihi are from Sobolev et al. (2007). Compared to olivines crystallized from partial melts of peridotite, olivine phenocrysts in the Hainan basalts have lower Ca and Mn, and higher Ni and Fe/Mn, indicating the involvement of pyroxenite in the mantle source.

the residual minerals for alkali basalts were mainly clinopyroxene, phlogopite and garnet, with the possible involvement of rutile. However, the geochemical features of the Hainan basalts presented here do not support this conclusion. Firstly, the CS-MS-A diagram for the tholeiites indicates that the residual minerals are dominated by Cpx and Gt with the possible involvement of Opx, but no Ol. Amphibole is unstable in the garnet-stability field ($P > 2$–2.5 GPa), therefore amphibole would not occur in the garnet-bearing mantle source of tholeiites. Also, lower Ca, Mn, higher Ni contents and Fe/Mn of olivines from the Hainan basalts than those from peridotite partial melts imply that there is no olivine in the source of the Hainan basalts (Herzberg, 2011). Secondly, the presence of phlogopite in the magma source would raise the bulk $D_{Rb,\ Ba,\ K}$, and this would lead to considerable variability in the ratios between alkali and alkaline earth elements and other incompatible elements. However the alkali basalts have nearly constant Rb/Nb (0.89 ± 0.14, 2σ), suggesting that phlogopite may not be present in the source region of alkali basalts. Furthermore, as Rb and Ba are compatible in amphibole and phlogopite, and Nb and Ta are compatible in rutile, if K-bearing minerals (amphibole or phlogopite) and rutile were residual in the mantle source of the Hainan basalts, the formed lavas would display negative Rb, Ba, Nb and Ta anomalies. However, in the tholeiites and alkali basalts from Hainan Island Rb, Ba, Nb and Ta all exhibit positive anomalies. Finally, experiments demonstrate that not only are Nb and Ta strongly compatible in rutile ($D^{rutile/melt}_{Nb,\ Ta} \gg 1$), but also that rutile fractionates Nb from Ta effectively, and thus melts in equilibrium with rutile have high Nb/Ta (Klemme et al., 2002, 2005; Xiong et al., 2005). If rutile was a residual mineral of the alkali basalts, but was not of the tholeiites, this would fractionate Nb from Ta in the alkali basalts. However, Nb/Ta in the alkali basalts (15.96 ± 0.94, 2σ) is extremely similar to those in the tholeiites (16.17 ± 1.00, 2σ). Therefore, we argue that there is no residual K-bearing mineral or rutile after melt extraction from the magma source of the alkali basalts.

Instead we infer that in the source of the tholeiites the residual minerals after melt extraction are mainly clinopyroxene and garnet, with the possible involvement of orthopyroxene, but without olivine or amphibole, at a melting pressure of ~3 GPa. In the source of the alkali basalts the residual minerals are mainly clinopyroxene and garnet, without the involvement of phlogopite or rutile. However, the melting pressure is hard to estimate because the alkali basalts plot in the field of a bimineralic eclogite source (Herzberg, 2011).

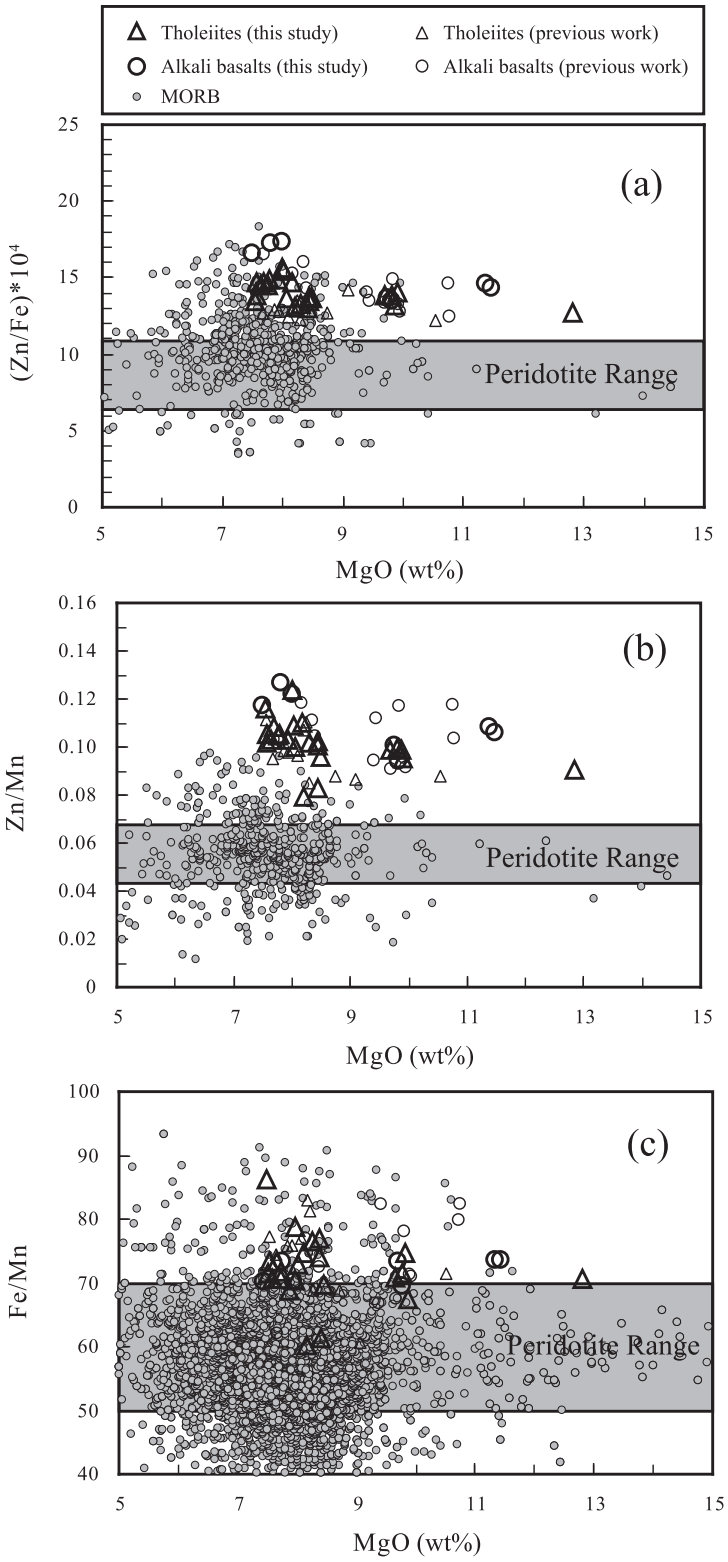

Fig. 15. Relationship between (a) Zn/Fe, (b) Zn/Mn and (c) Fe/Mn and MgO contents in Hainan tholeiites and alkali basalts with MgO >7.5%. Data of previous work is from Han et al. (2009), Zou and Fan (2010) and Wang et al. (2012). Field for peridotite is from Le Roux et al. (2010) and MORB is from PETDB database (http://petdb.ldeo.columbia.edu/petdb). Note that the Hainan basalts have higher Zn/Fe, Zn/Mn, and Fe/Mn than MORB and peridotites, which probably indicates the involvement of pyroxenite in their mantle source.

5.4.2. Lithology of mantle source

The upper mantle is composed of abundant peridotites, and work in the last few decades has attributed almost all of the basaltic lavas on Earth to melting of mantle peridotite (Yoder and Tilley, 1962; Green and Ringwood, 1963; O'Hara and Yoder, 1967; Hirose and Kushiro, 1993; Walter, 1998; Putirka, 2005; Rhodes et al., 2012). However, recent experimental studies indicate that partial melts of volatile-free mantle peridotite cannot match some key geochemical characteristics of intra-plate basalts, including their TiO_2, CaO, FeO^* and Al_2O_3 contents (Hirose and Kushiro, 1993; Walter, 1998; Hirschmann et al., 2003; Kogiso et al., 2003). As a result it has been proposed that intra-plate basalts could be derived from pyroxenite, peridotite + CO_2, and hornblendite source lithologies. For example, pyroxenite is invoked to be part of Hawaiian mantle source (Hauri, 1996; Ren et al., 2004, 2006, 2009; Sobolev et al., 2005, 2007; Herzberg, 2006, 2011). Sobolev et al. (2005, 2007) propose that an olivine-free pyroxenite served as the source lithology of the Hawaii shield basalts primarily on the basis that their olivine phenocrysts have lower Mn and Ca, and higher Ni and Fe/Mn than those crystallized from melts derived from a peridotite source. Herzberg (2006, 2011) and Herzberg and Asimow (2008) hold the view that, in contrast with partial melts of mantle peridotites, the lower CaO in the primary magma of Hawaii basalts also require pyroxenite as the source lithology. Dasgupta et al. (2007) suggest that low degree (1–5%) partial melts of metasomatic carbonated peridotites can match many compositional features of highly alkalic OIB. According to high-pressure melting experiments on hornblendite, clinopyroxene hornblendite, and hornblendite plus peridotite hybrids, Pilet et al. (2008, 2011) showed that partial melts of metasomatic hornblendite veins can reproduce key major and trace element characteristics of oceanic and continental alkaline magmas. Ratios of moderately incompatible trace elements and major elements, such as Fe/Mn (Humayun et al., 2004; Liu et al., 2008; Qin and Humayun, 2008; Le Roux et al., 2010, 2011), Zn/Fe and Zn/Mn (Le Roux et al., 2010, 2011), can be good indicators of the lithology and residual mineral assemblages of the magma source. Le Roux et al. (2010, 2011) indicate that Zn/Fe, Fe/Mn and Zn/Mn do not fractionate between olivine, orthopyroxene and partial melts, but are strongly fractionated when garnet or clinopyroxene are the dominant phases involved during melting or crystallization. Davis et al. (2013) experimentally determined mineral/melt partitioning of FRTE and then calculated model partial melts of peridotite. The results show that lower Co/Fe^*10^4 (<7), higher Fe/Mn (>62) and $(Zn/Fe)^*10^4$ (>13) are characteristic of non-peridotite source lithology of natural OIB. Therefore, partial melts of eclogite or garnet pyroxenite have higher Zn/Fe, Zn/Mn and Fe/Mn and lower Co/Fe than mantle peridotite.

As for the Hainan basalts, many geochemical features indicate that mantle peridotite cannot serve as the sole source lithology. First, compared to partial melts of peridotite, the Hainan basalts (including melt inclusions and whole rocks) have lower CaO contents (Fig. 12). Second, comparisons between the Hainan primary magmas and various experimental partial melts demonstrate that peridotite melts cannot match some key major elements compositions of the Hainan basalts, such as higher TiO_2, FeO^* and lower Na_2O/TiO_2, CaO/Al_2O_3 (Fig. 13). In addition, compared to olivines crystallized from partial melts of peridotite, olivine phenocrysts in the Hainan basalts have lower Ca and Mn, and higher Ni and Fe/Mn (Fig. 14). Lastly, Zn/Fe ($\times 10^4$), Zn/Mn and Fe/Mn of the Hainan basalts with MgO > 7.5 wt% are 14.4 ± 2, 0.1 ± 0.02, 72 ± 9, respectively (Fig. 15), higher than the range for MORB and peridotite (8.5 ± 0.9, 0.05 ± 0.006, 61 ± 5, respectively) (Le Roux et al., 2010), and the Co/Fe ($\times 10^4$) is 5.8 ± 0.9, lower than model peridotite melts (>7) (Davis et al., 2013). These evidences imply that non-peridotite components contribute to the mantle source of the Hainan basalts. Although partial melts of carbonated peridotites (peridotite + CO_2) can well match the moderate TiO_2 and Na_2O/TiO_2, they have slightly lower FeO^* and obviously higher CaO/Al_2O_3 than the Hainan basalts (Fig. 13). Pilet et al. (2008, 2011) point out that the partial melts of hornblendite are enriched in strongly incompatible elements, but depleted in K, Pb, Zr and Hf. Carbonatites are enriched in incompatible elements but depleted in K, Zr, Hf, Ti (Hoernle et al., 2002; Bizimis et al., 2003). Partial melts of carbonated mantle also display negative K, Zr, Hf and Ti anomalies (Hirose, 1997; Dasgupta et al., 2007). In spite of weakly negative Ti anomalies in the Hainan alkali basalts ($Ti/Ti^* = 0.57 \sim 1.07$), there are no obvious negative Zr, Hf and K anomalies (tholeiites: $Hf/Hf^* = 1.0 \pm 0.22$, alkali basalts: $Hf/Hf^* = 1.03 \pm 0.36$) in the primitive-mantle normalized trace element patterns for the Hainan basalts. Furthermore, Fe/Mn of hornblendite is 54.3 ± 8.2 (Pilet et al., 2008) and peridotite + CO_2 is 52.6 ± 18.2 (Dasgupta et al., 2007), both of which are much lower than that of the Hainan basalts. For these reasons, we hold the view that neither peridotite + CO_2 nor metasomatic hornblendite could serve as the source lithology of the Hainan basalts.

Instead we propose melting of an olivine-free pyroxenite contributes to the distinct geochemical characteristics of the Hainan basalts. While Ca is extremely incompatible in olivine ($D_{Ca}^{Ol} = 0.02$, Leeman and Scheidegger, 1977), the predominant rock-forming mineral of peridotite, it is compatible in clinopyroxene ($D_{Ca}^{Cpx} = 1.82$–1.95, Pertermann and Hirschmann, 2002), the main rock-forming mineral in pyroxenite. Therefore the CaO contents of partial melts of pyroxenite would be lower than that of peridotite melts, and this is consistent with the low CaO contents of the Hainan basalts (Fig. 12). In addition, experimental partial melts of garnet pyroxenite match the key major elements (TiO_2 and FeO^*) and major element ratios (Na_2O/TiO_2 and CaO/Al_2O_3) of the Hainan primary magmas (Fig. 13). Similar to Hawaii basalts, the olivine phenocrysts of the Hainan basalts have low Ca and Mn, and high Ni and Fe/Mn (Fig. 14), providing further evidence for contributions from pyroxenite components (Herzberg, 2011). Alkali basalts with MgO >7.5 wt% and all of the tholeiites have higher Zn/Fe, Zn/Mn and Fe/Mn (Fig. 15). Humayun et al. (2004) and Qin and Humayun (2008) attribute the high Fe/Mn of the Hawaiian basalts to Fe excess associated with core-mantle interactions. However, Zn content of the

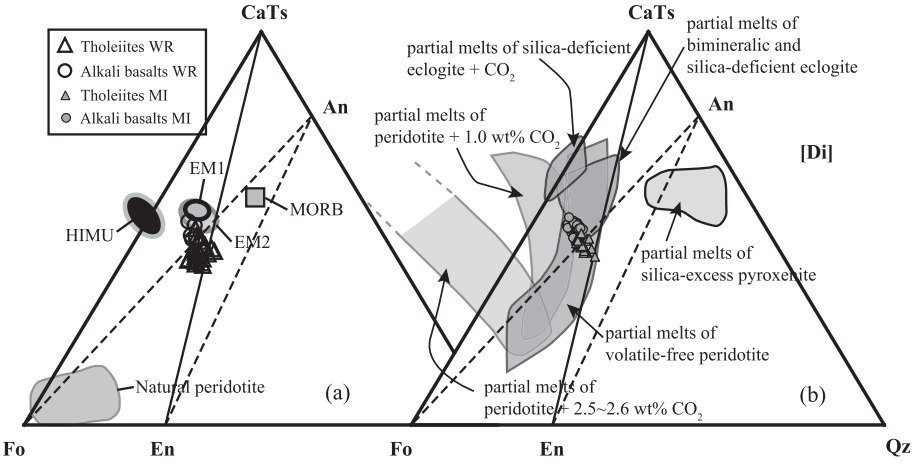

Fig. 16. CMAS projections of O'Hara (1968) showing normative compositions of whole rocks and melt inclusions for the Hainan basalts in the pseudoternary system forsterite (Fo: Mg_2SiO_4)-Ca-Tschermaks (CaTs: $CaAl_2SiO_6$)-quartz (Qtz: SiO_2), projected from diposide [Di]. Only olivine fractionation corrected primary magma compositions of whole rocks and melt inclusions with high MgO (15–19 wt%) are plotted. Also plotted for reference are average olivine fractionation corrected compositions of HIMU, EM1, EM2 and MORB, and fields for natural peridotite and various experiment partial melts, which are all modified from Jackson and Dasgupta (2008). This plot shows that the projection fields of melt inclusions are basically consistent with those of whole rocks. Primary melt compositions of alkaline whole rocks and melt inclusions are almost nepheline-normative, which fall above the Fo-An join, while those of tholeiitic whole rocks and melt inclusions are almost hypersthene, which fall below the Fo-An join. Nevertheless, both tholeiitic and alkalic compositions plot on the silica-poor side of the thermal divide (CaTs-En join), similar to that of EM1-EM2 compositions (see text for further explanation).

core is ~30 ppm (Corgne et al., 2008), lower than that in the Hainan basalts (~120 ppm), so any Zn contamination from the core is insignificant. Moreover, an excess in Fe from the core would decrease Zn/Fe, which is contrary to the higher Zn/Fe (Le Roux et al., 2010) in the Hainan basalts. So we explain the high Fe/Mn, Zn/Mn and Zn/Fe as reflecting the involvement of pyroxenite in the mantle source. Lastly, because La is more compatible relative to Nb in pyroxenite whereas the opposite is true for peridotite (Stracke and Bourdon, 2009), La/Nb of pyroxenite melts are much lower than those of peridotite melts. Stracke and Bourdon (2009) demonstrate that the combination of La/Nb $\ll 1$ with enriched isotopic signatures and deep melting signatures is perhaps the most conspicuous signature of melting mafic source components. Section 5.4.1 discussed that garnet may be involved in the residual minerals of the Hainan basalts, indicating melting of a deep mantle source (>75 km), and previous studies indicate that the Hainan basalts have enriched $^{87}Sr/^{86}Sr$, $^{143}Nd/^{144}Nd$ and Pb isotopic signatures (Tu et al., 1991; Flower et al., 1992; Han et al., 2009; Wang et al., 2013). La/Nb of tholeiites are 0.66–0.93 and those of alkali basalts are 0.60–0.74. Combining the above signatures, we argue that the pyroxenite was involved in the mantle source of the Hainan basalts.

5.4.3. Origin of the pyroxenite components in the mantle source

CMAS projections of the primary magma compositions for the melt inclusions from the Hainan basalts are consistent with those of the whole rocks (Fig. 16). Alkaline whole rocks and melt inclusions are almost nepheline-normative, falling above the Fo-An join; meanwhile tholeiitic whole rocks and melt inclusions are hypersthene-normative, falling below the Fo-An join. Additionally, all primary magma compositions fall on the silica-poor side of the En-CaTs join in the Fo-Qtz-CaTs pseudoternary, similar to EM1-EM2 compositions, indicating that the generation of the Hainan basalts involves a mantle source component that falls on the silica-poor side of the thermal divide (Kogiso et al., 2004; Jackson and Dasgupta, 2008). Thus, the Hainan basalts are likely to require a mantle source of volatile-free peridotite, or bimineralic and silica-deficient eclogite, rather than a metasomatized mantle source with CO_2-bearing eclogite and peridotite, or silica-excess pyroxenite. Although the CMAS projections of the Hainan tholeiites and alkali basalts suggest that they are derived from partial melts of volatile-free peridotite, as discussed above such a source cannot explain some key geochemical features of the basalts, such as the low CaO, Na_2O/TiO_2, CaO/Al_2O_3 and Co/Fe, high TiO_2, Fe/Mn, Zn/Mn, and Zn/Fe of whole rocks, and the low Ca and Mn and high Ni and Fe/Mn of their olivine phenocrysts.

The Hainan basalts display significant Sr positive anomalies (tholeiites: $(Sr/Nd)_{PM} = 1.40 \pm 0.24$, and alkali basalts: $(Sr/Nd)_{PM} = 1.27 \pm 0.25$) in the primitive mantle-normalized spidergrams (Fig. 6c, d), indicating a "plagioclase-rich gabbro" signature in the mantle source or plagioclase accumulation during magma evolution. However, very few plagioclase phenocrysts were observed in the tholeiites and their abundance was only ~5% in the alkali basalts. This suggests that the positive Sr anomalies are due to a "plagioclase-rich gabbro" signature in the source rather than plagioclase accumulation during magma evolution (Sobolev et al., 2000). Three main hypotheses have been proposed to explain the "plagioclase-rich gabbro" signature in source of intra-plate basalts: (1) the existence of a recycled plagioclase-rich cumulate (now eclogite) in the mantle source (Hofmann and Jochum, 1996; Chauvel

and Hémond, 2000; Sobolev et al., 2000), (2) the interaction of basalts with plagioclase-rich cumulates during melt percolation through the oceanic lithosphere in an oceanic intra-plate setting (Danyushevsky et al., 2004; Gurenko and Sobolev, 2006; Saal et al., 2007), and (3) assimilation of gneiss derived from continental crust in continental intra-plate settings. Having erupted in a continental intra-plate tectonic setting (Yan et al., 2008), the second hypothesis can be ruled out for the Hainan basalts and, as discussed in Section 5.3 there is little evidence for crustal contamination in the Hainan basalts (Zou and Fan, 2010). Therefore, we argue that a recycled gabbro component was involved in the source region of the Hainan basalts. In the primitive mantle-normalized spidergrams, the Hainan basalts display positive Rb and Ba, and negative Th and U anomalies, also indicating the involvement of recycled gabbro in the mantle source (Hofmann and Jochum, 1996). The presence of either subducted oceanic crust or delaminated lower continental crust in the magma source can explain the presence of recycled gabbro in the source region. The Hainan basalts display positive Nb and Ta anomalies in incompatible element spidergrams suggesting that delaminated lower continental crust was not present in the mantle source. Instead we argue that recycled subducted oceanic crust was involved in producing the Hainan basalts.

Assuming that the recycled oceanic crust remains isolated from the surrounding peridotite matrix during subduction into the mantle near the subduction zone, it will dehydrate and transform into a variety of clinopyroxene- and garnet-bearing assemblages, including quartz-, coesite-, or bimineralic eclogites (Kogiso et al., 1997; Pertermann and Hirschmann, 2003; Spandler et al., 2008), which are referred to as stage-1 pyroxenite by Herzberg (2011). High-pressure melting experiments performed by Kogiso and Hirschmann (2006) demonstrate that partial melts derived from bimineralic eclogite have low Al_2O_3 and high FeO, comparable to those of alkalic OIB, suggesting that bimineralic recycled crust is a potential source for alkalic OIB. However, the MgO content of the bimineralic eclogite-derived melts do not exceed 10–11 wt% (Kogiso and Hirschmann, 2006), which is much lower than that of olivine fractionation corrected primary magma composition of the Hainan basalts (15.25–17.39 wt% for tholeiites and 15.46–16.8 wt% for alkali basalts; Fig. 13). As a result, direct partial melting of subducted oceanic crust (in the form of bimineralic eclogite, stage-1 pyroxenite) cannot serve as the sole source, and the involvement of surrounding peridotite seems to be necessary to account for the high primary MgO contents. Owing to the lower melting points (at a given pressure) of crustal rocks compared to peridotite (Hirschmann and Stolper, 1996; Hirschmann, 2000; Yaxley, 2000; Kogiso et al., 2004), they could melt preferentially relative to ambient peridotitic mantle to produce a fluid/melt that is highly reactive with peridotite (Liu et al., 2008; Herzberg, 2011; Mallik and Dasgupta, 2012, 2013). High-pressure experiments have demonstrated that the reaction between melts derived from MORB-eclogite and fertile peridotite can consume olivine and generate orthopyroxene (Yaxley and Green, 1998; Rapp et al., 1999; Herzberg, 2011; Mallik and Dasgupta, 2012, 2013), producing a stage-2 pyroxenite. Hence, we hold the view that silica-deficient pyroxenite derived from melt–peridotite reaction, or mechanical mixing between recycled oceanic crust and peridotite, can serve as the source lithology of the Hainan basalts, producing partial melts that match their composition better than MORB-eclogite and fertile peridotite sources.

5.4.4. Partial melting of silica-deficient pyroxenite in the source region

Although the source lithology of tholeiites and alkali basalts are both pyroxenitic, they still have distinct geochemical characteristics: the tholeiites have higher SiO_2 and Al_2O_3, and lower Na_2O, K_2O and REE, whereas the alkali basalts contain lower SiO_2 and Al_2O_3, and higher Na_2O, K_2O and REE (Figs. 5 and 6). Because the Hainan basalts with MgO >7.5 wt% were not modified significantly during magmatic processes, the key differences in elemental geochemistry between the tholeiites and alkali basalts are likely to result from diverse pyroxenite sources (Kogiso et al., 2004; Zhang et al., 2009; Wang et al., 2011; Xu et al., 2012) or from different degrees of melting of a similar mantle source (Ito and Kennedy, 1974; Keshav et al., 2004). However, bulk-rock Sr–Nd–Pb–Os isotopic compositions (Tu et al., 1991; Flower et al., 1992; Han et al., 2009; Zou and Fan, 2010; Wang et al., 2013) in the Cenozoic Hainan tholeiites and alkali basalts exhibit little variation, which suggests that both the tholeiites and alkali basalts share a similar mantle source. The view that tholeiites and alkali basalts were derived from different degrees of melting of a similar mantle source was generally based on the premise that their mantle sources are peridotitic (McKenzie and O'nions, 1991). However, experimental studies demonstrate that the tholeiitic to alkalic basalt transition observed in ocean-island basalts can be reproduced by high-pressure melting experiments of eclogite nodules (Ito and Kennedy, 1974) or garnet clinopyroxenite (Keshav et al., 2004). Mallik and Dasgupta (2012) performed reaction experiments between MORB-eclogite derived melts and fertile peridotite to test the generation of ocean island basalts. In their experiments, melt was introduced either as a separate layer or mixed homogeneously with peridotite to simulate channelized and porous flow respectively. Experimental results show that they can also generate a continuous spectrum from tholeiitic to alkalic melts with increasing extent of wall–rock reaction in layered runs and decreasing melt/rock ratio in mixed experiments. Therefore, we suggest that the transition from tholeiitic to alkalic compositions in the Hainan basalts was generated by decreasing degrees of melting of a similar silica-deficient pyroxenite source, which is consistent with the lower incompatible trace element and REE abundances in the tholeiites compared to the alkali basalts (Figs. 6 and 7).

5.4.5. Magma mixing inferred from melt inclusions

Magma mixing refers to comingling of different magmas in different proportions to generate a series of transitional magmas. However, it is difficult to find direct evidence for magma mixing in whole rocks, because they represent only

an 'average' composition formed by a variety of complex processes including magma mixing in the mantle source (Sobolev, 1996; Ren et al., 2005). Melt inclusions trapped in early crystallizing olivine phenocrysts in the magma system can record these processes in the deep magma chamber (Sobolev, 1996; Sobolev et al., 2000; Ren et al., 2005; Kent, 2008). We believe that the compositional range exhibited by the Hainan basalts was derived from decreasing degrees of melting of a similar silica-deficient pyroxenite from the tholeiitic to alkalic basalts. As the range is continuous it can be interpreted to be due to the quick expansion of the eclogite "surface" from the tholeiitic part of the basalt tetrahedron into the alkalic part of the tetrahedron (Keshav et al., 2004). However, in the process of melt evolution due to crystallization, primary magmas of high-Si tholeiitic melts and low-Si alkalic melts will be located on opposite sides of the thermal divide (the divide in Fig. 1b of Herzberg (2011)) and belong to different evolutionary series. Hence, during natural cooling, one magma series cannot translate into the other through crystal differentiation. In addition, the chemical compositions of the erupted tholeiitic melts are hypersthene-normative while those of the alkaline melts are nepheline-normative. These cannot occur together in a single sample without magmatic processes in addition to crystallization affecting the samples. Subalkaline and alkaline basaltic melt inclusions have been found within olivine phenocrysts from the alkali basalts (YX-1 and YX-4, Fig. 4a, b) and the tholeiites (BP-5 and ZT-2, Fig. 4c, d). This indicates that the Hainan basalts may have experienced a series of complex processes in the deep magma chamber prior to eruption, possibly including magma mixing.

Therefore, we speculate that there was a deep magma chamber below the Hainan Island, which was supplied by high-Si melts and low-Si melts derived from different degrees of melting of a silica-deficient pyroxenite. For the overwhelming majority of the Hainan basalts no magma mixing and perturbation occurred and the olivine that crystallized from high-Si melts trapped subalkaline melts, while the olivine that crystallized from low-Si melts trapped alkali melts. In a few cases magma mixing and perturbation did occur, in which case the olivines that crystallized from high-Si melts trapped both subalkaline and alkaline melts, and finally formed phenocrysts in the tholeiitic basalts (BP-5, ZT-2). Olivines that crystallized from low-Si melts also trapped both subalkaline and alkali melts, but finally formed phenocrysts in the alkalic basalts (YX-1, YX-4).

6. CONCLUSIONS

Cenozoic basalts erupted in North Hainan Island are predominantly tholeiites with a small number of alkali basalts. They show little evidence of post-eruption alteration or crustal contamination. Petrographic observations and chemical compositions of whole rocks indicate that alkali basalts with MgO >7.5 wt% and all the tholeiites only experienced fractionation of olivine, whereas clinopyroxene, plagioclase, even Fe–Ti oxides started to fractionate in the alkali basalts with MgO <7.5 wt%. Combining CS-MS-A diagrams and other geochemical characteristics of the Hainan basalts, we argue that the residual minerals for the tholeiitic basalts are mainly clinopyroxene and garnet, with the possible involvement of orthopyroxene, but without olivine or amphibole, and suggest a melting pressure of ~3 GPa. However, the residual minerals for the alkali basalts are solely clinopyroxene and garnet, without the involvement of phlogopite or rutile, but the melting pressure is hard to estimate. Compared to the partial melts of peridotite, the Hainan basalts have lower CaO, Na_2O/TiO_2, CaO/Al_2O_3 and Co/Fe, and higher TiO_2, FeO^*, Fe/Mn, Zn/Fe and Zn/Mn. Meanwhile, compared to olivines crystallized from partial melts of peridotite, olivines in the Hainan basalts have lower Ca and Mn, and higher Ni and Fe/Mn. All of these features indicate that pyroxenite is involved in the mantle source of the Hainan basalts. CMAS projections of the primary magma compositions of the Hainan basalts indicate that the stage-2 silica-deficient pyroxenite derived from melt–peridotite reaction or mechanical mixing between recycled oceanic crust and peridotite can serve as the source lithology. The resultant partial melts better match the composition of the Hainan basalts than those of MORB-eclogite and fertile peridotite. The transition from tholeiitic to alkalic basalts can be ascribed to decreasing degrees of melting of a similar silica-deficient pyroxenite source. Subalkaline and alkaline basaltic melt inclusions have been found in a single sample, indicating that magma mixing had occurred in the deep magma chamber prior to erupting below the Hainan Island.

ACKNOWLEDGEMENTS

We are grateful to L. Wu for her assistance in the field trip and preparing and analyzing the melt inclusions and olivines. We thank Y. Liu, G. Q. Hu, and X. L. Tu for their assistance with major and trace elements analyses of the bulk rocks. We also gratefully acknowledge the helpful comments by the associate editor Andreas Stracke, Claude Herzberg and two anonymous reviewers. This work was supported by the "hundred talent project" of Chinese Academy of Sciences, the National Science Foundation of China (91128203, 41172064). This is contribution No. 2009 from GIG-CAS.

APPENDIX A. SUPPLEMENTARY DATA

Supplementary data associated with this article can be found, in the online version, at http://dx.doi.org/10.1016/j.gca.2014.12.023.

REFERENCES

Bizimis M., Salters V. J. and Dawson J. B. (2003) The brevity of carbonatite sources in the mantle: evidence from Hf isotopes. *Contrib. Mineral. Petrol.* **145**, 281–300.

Chauvel C. and Hémond C. (2000) Melting of a complete section of recycled oceanic crust: trace element and Pb isotopic evidence from Iceland. *Geochem. Geophys. Geosyst.* **1**. http://dx.doi.org/10.1029/1999GC000002, 1001.

Chauvel C., McDonough W., Guille G. and Duncan R. (1997) Contrasting old and young volcanism in Rurutu Island, Austral chain. *Chem. Geol.* **139**, 125–143.

Chauvel C., Lewin E., Carpentier M., Arndt N. T. and Marini J. C. (2007) Role of recycled oceanic basalt and sediment in generating the Hf–Nd mantle array. *Nat. Geosci.* **1**, 64–67.

Chung S. L., Sun S., Tu K., Chen C. H. and Lee C. Y. (1994) Late Cenozoic basaltic volcanism around the Taiwan Strait, SE China: product of lithosphere–asthenosphere interaction during continental extension. *Chem. Geol.* **112**, 1–20.

Chung S. L., Jahn B. M., Chen S. J., Lee T. and Chen C. H. (1995) Miocene basalts in northwestern Taiwan: evidence for EM-type mantle sources in the continental lithosphere. *Geochim. Cosmochim. Acta* **59**, 549–555.

Chung S. L., Cheng H., Jahn B., O'Reilly S. Y. and Zhu B. (1997) Major and trace element, and Sr–Nd isotope constraints on the origin of Paleogene volcanism in South China prior to the South China Sea opening. *Lithos* **40**, 203–220.

Corgne A., Keshav S., Wood B. J., McDonough W. F. and Fei Y. (2008) Metal–silicate partitioning and constraints on core composition and oxygen fugacity during Earth accretion. *Geochim. Cosmochim. Acta* **72**, 574–589.

Cox K. G. (1980) A model for flood basalt volcanism. *J. Petrol.* **21**, 629–650.

Danyushevsky L. V. (2001) The effect of small amounts of H_2O on crystallisation of mid-ocean ridge and backarc basin magmas. *J. Volcanol. Geoth. Res.* **110**, 265–280.

Danyushevsky L. V. and Plechov P. (2011) Petrolog 3: integrated software for modeling crystallization processes. *Geochem. Geophys. Geosyst.* **12**. http://dx.doi.org/10.1029/2011GC003516.

Danyushevsky L. V., Della-Pasqua F. N. and Sokolov S. (2000) Re-equilibration of melt inclusions trapped by magnesian olivine phenocrysts from subduction-related magmas: petrological implications. *Contrib. Mineral. Petrol.* **138**, 68–83.

Danyushevsky L. V., Sokolov S. and Falloon T. J. (2002) Melt inclusions in olivine phenocrysts: using diffusive re-equilibration to determine the cooling history of a crystal, with implications for the origin of olivine-phyric volcanic rocks. *J. Petrol.* **43**, 1651–1671.

Danyushevsky L. V., Leslie R. A. J., Crawford A. J. and Durance P. (2004) Melt inclusions in primitive olivine phenocrysts: the role of localized reaction processes in the origin of anomalous compositions. *J. Petrol.* **45**, 2531–2553.

Dasgupta R., Hirschmann M. M. and Stalker K. (2006) Immiscible transition from carbonate-rich to silicate-rich melts in the 3 GPa melting interval of eclogite + CO_2 and genesis of silica-undersaturated oceanic island lavas. *J. Petrol.* **47**, 647–671.

Dasgupta R., Hirschmann M. M. and Smith N. D. (2007) Partial melting experiments of peridotite + CO_2 at 3 GPa and genesis of alkalic ocean island basalts. *J. Petrol.* **48**, 2093–2124.

Davis F. A., Humayun M., Hirschmann M. M. and Cooper R. S. (2013) Experimentally determined mineral/melt partitioning of first-row transition elements (FRTE) during partial melting of peridotite at 3 GPa. *Geochim. Cosmochim. Acta* **104**, 232–260.

Fan Q. C. and Hooper P. R. (1989) The mineral chemistry of ultramafic xenoliths of Eastern China: implications for upper mantle composition and the paleogeotherms. *J. Petrol.* **30**, 1117–1158.

Fan Q. C. and Hooper P. R. (1991) The Cenozoic basaltic rocks of Eastern China – petrology and chemical-composition. *J. Petrol.* **32**, 765–810.

Fan Q. C., Sun Q., Li N. and Sui J. L. (2004) Periods of volcanic activity and magma evolution of Holocene in North Hainan Island. *Acta Petrol. Sin.* **20**, 533–544 (in Chinese with English abstract).

Fedorov P. I. and Koloskov A. V. (2005) Cenozoic volcanism of Southeast Asia. *Petrology* **13**, 352–380.

Flower M. F. J., Zhang M., Chen C. Y., Tu K. and Xie G. H. (1992) Magmatism in the south China basin: 2. Post-spreading Quaternary basalts from Hainan Island, south China. *Chem. Geol.* **97**, 65–87.

Ford C. E., Russell D. G., Craven J. A. and Fisk M. R. (1983) Olivine-liquid equilibria: temperature, pressure and composition dependence of the crystal/liquid cation partition coefficients for Mg, Fe^{2+}, Ca and Mn. *J. Petrol.* **24**, 256–266.

Gaetani G. A. and Watson E. B. (2002) Modeling the major-element evolution of olivine-hosted melt inclusions. *Chem. Geol.* **183**, 25–41.

Gao S., Rudnick R. L., Yuan H. L., Liu X. M., Liu Y. S., Xu W. L., Ling W. L., Ayers J., Wang X. C. and Wang Q. H. (2004) Recycling lower continental crust in the North China craton. *Nature* **432**, 892–897.

Goto A. and Tatsumi Y. (1996) Quantitative analysis of rock samples by an X-ray fluorescence spectrometer (II). *Rigaku J.* **13**, 20–38.

Green D. and Ringwood A. (1963) Mineral assemblages in a model mantle composition. *J. Geophys. Res.* **68**, 937–945.

Gurenko A. A. and Sobolev A. V. (2006) Crust–primitive magma interaction beneath neovolcanic rift zone of Iceland recorded in gabbro xenoliths from Midfell, SW Iceland. *Contrib. Mineral. Petrol.* **151**, 495–520.

Halliday A. N., Lee D. C., Tommasini S., Davies G. R., Paslick C. R., Fitton J. G. and James D. E. (1995) Incompatible trace-elements in OIB and MORB and source enrichment in the sub-oceanic mantle. *Earth Planet. Sci. Lett.* **133**, 379–395.

Han J. W., Xiong X. L. and Zhu Z. Y. (2009) Geochemistry of Late-Cenozoic basalts from Leiqiong area: the origin of EM2 and the contributions from sub-continental lithosphere mantle. *Acta Petrol. Sin.* **25**, 3208–3220 (in Chinese with English abstract).

Hauri E. H. (1996) Major-element variability in the Hawaiian mantle plume. *Nature* **382**, 415–419.

Hauri E. H., Kent A. J. R. and Arndt N. (2002) Melt inclusions at the millennium: toward a deeper understanding of magmatic processes – preface. *Chem. Geol.* **183**, 1–3.

Herzberg C. (2006) Petrology and thermal structure of the Hawaiian plume from Mauna Kea volcano. *Nature* **444**, 605–609.

Herzberg C. (2011) Identification of source Lithology in the Hawaiian and Canary Islands: implications for origins. *J. Petrol.* **52**, 113–146.

Herzberg C. and Asimow P. D. (2008) Petrology of some oceanic island basalts: PRIMELT2. XLS software for primary magma calculation. *Geochem. Geophys. Geosyst.* **9**. http://dx.doi.org/10.1029/2008GC002057.

Hirose K. (1997) Partial melt compositions of carbonated peridotite at 3 GPa and role of CO_2 in alkali-basalt magma generation. *Geophys. Res. Lett.* **24**, 2837–2840.

Hirose K. and Kushiro I. (1993) Partial melting of dry peridotites at high pressures: determination of compositions of melts segregated from peridotite using aggregates of diamond. *Earth Planet. Sci. Lett.* **114**, 477–489.

Hirschmann M. M. (2000) Mantle solidus: experimental constraints and the effects of peridotite composition. *Geochem. Geophys. Geosyst.* **1**. http://dx.doi.org/10.1029/2000GC000070.

Hirschmann M. M. and Stolper E. M. (1996) A possible role for garnet pyroxenite in the origin of the "garnet signature" in MORB. *Contrib. Mineral. Petrol.* **124**, 185–208.

Hirschmann M. M., Kogiso T., Baker M. B. and Stolper E. M. (2003) Alkalic magmas generated by partial melting of garnet pyroxenite. *Geology* **31**, 481–484.

Ho K. S., Chen J. and Juang W. (2000) Geochronology and geochemistry of late Cenozoic basalts from the Leiqiong area, southern China. *J. Asian Earth Sci.* **18**, 307–324.

Ho K. S., Chen J., Lo C. and Zhao H. (2003) ^{40}Ar–^{39}Ar dating and geochemical characteristics of late Cenozoic basaltic rocks from the Zhejiang-Fujian region, SE China: eruption ages, magma evolution and petrogenesis. *Chem. Geol.* **197**, 287–318.

Hoang N. and Flower M. (1998) Petrogenesis of Cenozoic basalts from Vietnam: implication for origins of a 'diffuse igneous province'. *J. Petrol.* **39**, 369–395.

Hoang N., Flower M. and Carlson R. (1996) Major, trace element, and isotopic compositions of Vietnamese basalts: interaction of hydrous EM1-rich asthenosphere with thinned Eurasian lithosphere. *Geochim. Cosmochim. Acta* **60**, 4329–4351.

Hoernle K., Tilton G., Le Bas M. J., Duggen S. and Garbe-Schönberg D. (2002) Geochemistry of oceanic carbonatites compared with continental carbonatites: mantle recycling of oceanic crustal carbonate. *Contrib. Mineral. Petrol.* **142**, 520–542.

Hofmann A. W. (1997) Mantle geochemistry: the message from oceanic volcanism. *Nature* **385**, 219–229.

Hofmann A. W. and Jochum K. P. (1996) Source characteristics derived from very incompatible trace elements in Mauna Loa and Mauna Kea basalts, Hawaii Scientific Drilling Project. *J. Geophys. Res.: Solid Earth* **101**, 11831–11839.

Hofmann A. W. and White W. M. (1982) Mantle plumes from ancient oceanic-crust. *Earth Planet. Sci. Lett.* **57**, 421–436.

Hofmann A. W., Jochum K. P., Seufert M. and White W. M. (1986) Nb and Pb in Oceanic basalts – new constraints on mantle evolution. *Earth Planet. Sci. Lett.* **79**, 33–45.

Humayun M., Qin L. and Norman M. D. (2004) Geochemical evidence for excess iron in the mantle beneath Hawaii. *Science* **306**, 91–94.

Ito K. and Kennedy G. C. (1974) The composition of liquids formed by partial melting of eclogites at high temperatures and pressures. *J. Geol.*, 383–392

Jackson M. G. and Dasgupta R. (2008) Compositions of HIMU, EM1, and EM2 from global trends between radiogenic isotopes and major elements in ocean island basalts. *Earth Planet. Sci. Lett.* **276**, 175–186.

Kamenetsky V. and Crawford A. J. (1998) Melt–peridotite reaction recorded in the chemistry of spinel and melt inclusions in basalt from 43°N, Mid-Atlantic Ridge. *Earth Planet. Sci. Lett.* **164**, 345–352.

Kent A. J. R. (2008) Melt inclusions in basaltic and related volcanic rocks. *Rev. Mineral. Geochem.* **69**, 273–331.

Keshav S., Gudfinnsson G. H., Sen G. and Fei Y. (2004) High-pressure melting experiments on garnet clinopyroxenite and the alkalic to tholeiitic transition in ocean-island basalts. *Earth Planet. Sci. Lett.* **223**, 365–379.

Klemme S., Blundy J. D. and Wood B. J. (2002) Experimental constraints on major and trace element partitioning during partial melting of eclogite. *Geochim. Cosmochim. Acta* **66**, 3109–3123.

Klemme S., Prowatke S., Hametner K. and Günther D. (2005) Partitioning of trace elements between rutile and silicate melts: implications for subduction zones. *Geochim. Cosmochim. Acta* **69**, 2361–2371.

Kogiso T. and Hirschmann M. M. (2006) Partial melting experiments of bimineralic eclogite and the role of recycled mafic oceanic crust in the genesis of ocean island basalts. *Earth Planet. Sci. Lett.* **249**, 188–199.

Kogiso T., Tatsumi Y. and Nakano S. (1997) Trace element transport during dehydration processes in the subducted oceanic crust. 1. Experiments and implications for the origin of ocean island basalts. *Earth Planet. Sci. Lett.* **148**, 193–205.

Kogiso T., Hirschmann M. M. and Frost D. J. (2003) High-pressure partial melting of garnet pyroxenite: possible mafic lithologies in the source of ocean island basalts. *Earth Planet. Sci. Lett.* **216**, 603–617.

Kogiso T., Hirschmann M. M. and Pertermann M. (2004) High-pressure partial melting of mafic lithologies in the mantle. *J. Petrol.* **45**, 2407–2422.

Laporte D., Toplis M. J., Seyler M. and Devidal J. L. (2004) A new experimental technique for extracting liquids from peridotite at very low degrees of melting: application to partial melting of depleted peridotite. *Contrib. Mineral. Petrol.* **14**, 463–484.

Lassiter J. C. and Hauri E. H. (1998) Osmium-isotope variations in Hawaiian lavas: evidence for recycled oceanic lithosphere in the Hawaiian plume. *Earth Planet. Sci. Lett.* **164**, 483–496.

Le Bas M., Le Maitre R., Streckeisen A. and Zanettin B. (1986) A chemical classification of volcanic rocks based on the total alkali-silica diagram. *J. Petrol.* **27**, 745–750.

Le Roux V., Lee C. T. A. and Turner S. (2010) Zn/Fe systematics in mafic and ultramafic systems: implications for detecting major element heterogeneities in the Earth's mantle. *Geochim. Cosmochim. Acta* **74**, 2779–2796.

Le Roux V., Dasgupta R. and Lee C. T. A. (2011) Mineralogical heterogeneities in the Earth's mantle: constraints from Mn Co, Ni and Zn partitioning during partial melting. *Earth Planet. Sci. Lett.* **307**, 395–408.

Leeman W. and Scheidegger K. (1977) Olivine/liquid distribution coefficients and a test for crystal–iquid equilibrium. *Earth Planet. Sci. Lett.* **35**, 247–257.

Lei J. S., Zhao D. P., Steinberger B., Wu B., Shen F. L. and Li Z. X. (2009) New seismic constraints on the upper mantle structure of the Hainan plume. *Phys. Earth Planet. Inter.* **173**, 33–50.

Liu Y., Liu H. and Li X. H. (1996) Simultaneous and precise determination of 40 trace elements in rock samples using ICP-MS. *Geochimica* **25**, 552–558.

Liu Y. S., Gao S., Kelemen P. B. and Xu W. L. (2008) Recycled crust controls contrasting source compositions of Mesozoic and Cenozoic basalts in the North China Craton. *Geochim. Cosmochim. Acta* **72**, 2349–2376.

Long W. G., Lin Y. H., Shi C., Zhou J. B. and Lu C. Y. (2006a) Revision of the Pleistocene Daotang Formation in north Hainan Island, China. *Geol. Bull. China* **25**, 469–474 (in Chinese with English abstract).

Long W. G., Lin Y. H., Zhu Y. H., Shi C., Zhou J. B. and Lu C. Y. (2006b) Establishment of the early-mid-Pleistocene Duowen Formation on north Hainan Island, China. *Geol. Bull. China* **25**, 408–414 (in Chinese with English abstract).

Mallik A. and Dasgupta R. (2012) Reaction between MORB-eclogite derived melts and fertile peridotite and generation of ocean island basalts. *Earth Planet. Sci. Lett.* **329**, 97–108.

Mallik A. and Dasgupta R. (2013) Reactive infiltration of MORB-eclogite-derived carbonated silicate melt into fertile peridotite at 3 GPa and genesis of alkalic magmas. *J. Petrol.* **54**, 2267–2300.

McDonough W. F. and Sun S. S. (1995) The composition of the Earth. *Chem. Geol.* **120**, 223–253.

Mckenzie D. and Bickle M. J. (1988) The volume and composition of melt generated by extension of the lithosphere. *J. Petrol.* **29**, 625–679.

McKenzie D. and O'nions R. (1991) Partial melt distributions from inversion of rare earth element concentrations. *J. Petrol.* **32**, 1021–1091.

Niu Y. L. and O'Hara M. J. (2003) Origin of ocean island basalts: a new perspective from petrology, geochemistry, and mineral physics considerations. *J. Geophys. Res.* **108**. http://dx.doi.org/10.1029/2002JB002048.

Norman M. D., Garcia M. O., Kamenetsky V. S. and Nielsen R. L. (2002) Olivine-hosted melt inclusions in Hawaiian picrites:

equilibration melting, and plume source characteristics. *Chem. Geol.* **183**, 143–168.
O'Hara M. (1968) The bearing of phase equilibria studies in synthetic and natural systems on the origin and evolution of basic and ultrabasic rocks. *Earth-Sci. Rev.* **4**, 69–133.
O'Hara M. and Yoder H. (1967) Formation and fractionation of basic magmas at high pressures. *Scott. J. Geol.* **3**, 67–117.
Pertermann M. and Hirschmann M. M. (2002) Trace-element partitioning between vacancy-rich eclogitic clinopyroxene and silicate melt. *Am. Mineral.* **87**, 1365–1376.
Pertermann M. and Hirschmann M. M. (2003) Anhydrous partial melting experiments on MORB-like eclogite: phase relations, phase compositions and mineral-melt partitioning of major elements at 2–3 GPa. *J. Petrol.* **44**, 2173–2201.
Pilet S., Hernandez J., Bussy F. and Sylvester P. (2004) Short-term metasomatic control of Nb/Th ratios in the mantle sources of intraplate basalts. *Geology* **32**, 113–116.
Pilet S., Baker M. B. and Stolper E. M. (2008) Metasomatized lithosphere and the origin of alkaline lavas. *Science* **320**, 916–919.
Pilet S., Baker M. B., Müntener O. and Stolper E. M. (2011) Monte Carlo simulations of metasomatic enrichment in the lithosphere and implications for the source of alkaline basalts. *J. Petrol.* **52**, 1415–1442.
Putirka K. D. (2005) Mantle potential temperatures at Hawaii, Iceland, and the mid-ocean ridge system, as inferred from olivine phenocrysts: evidence for thermally driven mantle plumes. *Geochem. Geophys. Geosyst.* **6**. http://dx.doi.org/10.1029/2005GC000915.
Qin L. and Humayun M. (2008) The Fe/Mn ratio in MORB and OIB determined by ICP-MS. *Geochim. Cosmochim. Acta* **72**, 1660–1677.
Rapp R., Shimizu N., Norman M. and Applegate G. (1999) Reaction between slab-derived melts and peridotite in the mantle wedge: experimental constraints at 3.8 GPa. *Chem. Geol.* **160**, 335–356.
Ren Z. Y., Takahashi E., Orihashi Y. and Johnson K. T. M. (2004) Petrogenesis of tholeiitic lavas from the submarine Hana Ridge, Haleakala Volcano, Hawaii. *J. Petrol.* **45**, 2067–2099.
Ren Z. Y., Ingle S., Takahashi E., Hirano N. and Hirata T. (2005) The chemical structure of the Hawaiian mantle plume. *Nature* **436**, 837–840.
Ren Z. Y., Shibata T., Yoshikawa M., Johnson K. T. M. and Takahashi E. (2006) Isotope compositions of submarine Hana Ridge lavas, Haleakala volcano, Hawaii: implications for source compositions, melting process and the structure of the Hawaiian plume. *J. Petrol.* **47**, 255–275.
Ren Z. Y., Hanyu T., Miyazaki T., Chang Q., Kawabata H., Takahashi T., Hirahara Y., Nichols A. R. L. and Tatsumi Y. (2009) Geochemical differences of the Hawaiian shield lavas: implications for melting process in the heterogeneous Hawaiian plume. *J. Petrol.* **50**, 1553–1573.
Rhodes J. M., Huang S., Frey F. A., Pringle M. and Xu G. (2012) Compositional diversity of Mauna Kea shield lavas recovered by the Hawaii Scientific Drilling Project: inferences on source lithology, magma supply, and the role of multiple volcanoes. *Geochem. Geophys. Geosyst.* **13**. http://dx.doi.org/10.1029/2011GC003812.
Roeder P. and Emslie R. F. (1970) Olivine–liquid equilibrium. *Contrib. Mineral. Petrol.* **29**, 275–289.
Rudnick R. L. and Gao S. (2003) Composition of the continental crust. *Treatise Geochem.* **3**, 1–64.
Saal A., Hart S., Shimizu N., Hauri E. and Layne G. (1998) Pb isotopic variability in melt inclusions from oceanic island basalts, Polynesia. *Science* **282**, 1481–1484.
Saal A., Kurz M., Hart S., Blusztajn J., Blichert-Toft J., Liang Y. and Geist D. (2007) The role of lithospheric gabbros on the composition of Galapagos lavas. *Earth Planet. Sci. Lett.* **257**, 391–406.
Schwab B. E. and Johnston A. D. (2001) Melting systematics of modally variable, compositionally intermediate peridotites and the effects of mineral fertility. *J. Petrol.* **42**, 789–1811.
Sobolev A. V. (1996) Melt inclusions in minerals as a source of principle petrological information. *Petrology* **4**, 209–220.
Sobolev A. V., Hofmann A. W. and Nikogosian I. K. (2000) Recycled oceanic crust observed in 'ghost plagioclase' within the source of Mauna Loa lavas. *Nature* **404**, 986–990.
Sobolev A. V., Hofmann A. W., Sobolev S. V. and Nikogosian I. K. (2005) An olivine-free mantle source of Hawaiian shield basalts. *Nature* **434**, 590–597.
Sobolev A. V., Hofmann A. W., Kuzmin D. V., Yaxley G. M., Arndt N. T., Chung S. L., Danyushevsky L. V., Elliott T., Frey F. A., Garcia M. O., Gurenko A. A., Kamenetsky V. S., Kerr A. C., Krivolutskaya N. A., Matvienkov V. V., Nikogosian I. K., Rocholl A., Sigurdsson I. A., Sushchevskaya N. M. and Teklay M. (2007) The amount of recycled crust in sources of mantle-derived melts. *Science* **316**, 412–417.
Sobolev A. V., Hofmann A. W., Brugmann G., Batanova V. G. and Kuzmin D. V. (2008) A quantitative link between recycling and osmium isotopes. *Science* **321**, 536-536.
Spandler C., Yaxley G., Green D. H. and Rosenthal A. (2008) Phase relations and melting of anhydrous K-bearing eclogite from 1200 to 1600 °C and 3 to 5 GPa. *J. Petrol.* **49**, 771–795.
Stracke A. and Bourdon B. (2009) The importance of melt extraction for tracing mantle heterogeneity. *Geochim. Cosmochim. Acta* **73**, 218–238.
Sun S. S. and McDonough W. F. (1989) Chemical and isotopic systematics of oceanic basalts: implications for mantle composition and processes. *Geol. Soc. Lond., Spec. Publ.* **42**, 313–345.
Sun Z., Zhong Z. H., Keep M., Zhou D., Cai D. S., Li X. S., Wu S. M. and Jiang J. Q. (2009) 3D analogue modeling of the South China Sea: a discussion on breakup pattern. *J. Asian Earth Sci.* **34**, 544–556.
Swanson D. A. (1972) Magma supply rate at Kilauea Volcano, 1952–1971. *Science* **175**, 169–170.
Thompson R. and Gibson S. (2000) Transient high temperatures in mantle plume heads inferred from magnesian olivines in Phanerozoic picrites. *Nature* **407**, 502–506.
Tu K., Flower M. F. J., Carlson R. W., Zhang M. and Xie G. H. (1991) Sr, Nd, and Pb isotopic compositions of Hainan basalts (south China): implications for a subcontinental lithosphere Dupal source. *Geology* **19**, 567–569.
Walter M. J. (1998) Melting of garnet peridotite and the origin of komatiite and depleted lithosphere. *J. Petrol.* **39**, 29–60.
Wang Z. R. and Gaetani G. A. (2008) Partitioning of Ni between olivine and siliceous eclogite partial melt: experimental constraints on the mantle source of Hawaiian basalts. *Contrib. Mineral. Petrol.* **156**, 661–678.
Wang Y., Zhao Z. F., Zheng Y. F. and Zhang J. J. (2011) Geochemical constraints on the nature of mantle source for Cenozoic continental basalts in east-central China. *Lithos* **125**, 940–955.
Wang X. C., Li Z. X., Li X. H., Li J., Liu Y., Long W. G., Zhou J. B. and Wang F. (2012) Temperature, pressure, and composition of the mantle source region of Late Cenozoic basalts in Hainan Island, SE Asia: a consequence of a young thermal mantle plume close to subduction zones? *J. Petrol.* **53**, 177–233.
Wang X. C., Li Z. X., Li X. H., Li J., Xu Y. G. and Li X. H. (2013) Identification of an ancient mantle reservoir and young recycled materials in the source region of a young mantle plume:

implications for potential linkages between plume and plate tectonics. *Earth Planet. Sci. Lett.* **377**, 248–259.

Wasylenki L. E., Baker M. B., Kent J. R. A. and Stolper E. M. (2003) Near-solidus melting of the shallow upper mantle: partial melting experiments on depleted peridotite. *J. Petrol.* **44**, 1163–1191.

Willbold M. and Stracke A. (2006) Trace element composition of mantle end-members: implications for recycling of oceanic and upper and lower continental crust. *Geochem. Geophys. Geosyst.* **7**. http://dx.doi.org/10.1029/2005GC001005.

Workman R. K., Hart S. R., Jackson M., Regelous M., Farley K. A., Blusztajn J., Kurz M. and Staudigel H. (2004) Recycled metasomatized lithosphere as the origin of the enriched mantle II (EM2) end-member: evidence from the Samoan volcanic chain. *Geochem. Geophys. Geosyst.* **5**. http://dx.doi.org/10.1029/2003GC000623.

Xiong X. L., Adam J. and Green T. (2005) Rutile stability and rutile/melt HFSE partitioning during partial melting of hydrous basalt: implications for TTG genesis. *Chem. Geol.* **218**, 339–359.

Xu X. S., O'Reilly S. Y., Griffin W. L. and Zhou X. M. (2003) Enrichment of upper mantle peridotite: petrological, trace element and isotopic evidence in xenoliths from SE China. *Chem. Geol.* **198**, 163–188.

Xu Z., Zhao Z. F. and Zheng Y. F. (2012) Slab–mantle interaction for thinning of cratonic lithospheric mantle in North China: geochemical evidence from Cenozoic continental basalts in central Shandong. *Lithos* **146**, 202–217.

Yan Q. S., Shi X. F., Wang K. S., Bu W. R. and Xiao L. (2008) Major element, trace element, and Sr, Nd and Pb isotope studies of Cenozoic basalts from the South China Sea. *Sci. China, Ser. D: Earth Sci.* **51**, 550–566.

Yaxley G. M. (2000) Experimental study of the phase and melting relations of homogeneous basalt + peridotite mixtures and implications for the petrogenesis of flood basalts. *Contrib. Mineral. Petrol.* **139**, 326–338.

Yaxley G. M. and Green D. H. (1998) Reactions between eclogite and peridotite: mantle refertilisation by subduction of oceanic crust. *Schweiz. Mineral. Petrogr. Mitt.* **78**, 243–255.

Yoder H. S. and Tilley C. E. (1962) Origin of basalt magmas – an experimental study of natural and synthetic rock systems. *J. Petrol.* **3**, 342–532.

Zeng G., Chen L. H., Xu X. S., Jiang S. Y. and Hofmann A. W. (2010) Carbonated mantle sources for Cenozoic intra-plate alkaline basalts in Shandong, North China. *Chem. Geol.* **273**, 35–45.

Zhang M., Tu K., Xie G. H. and Flower M. F. J. (1996) Subduction-modified subcontinental mantle in South China: trace element and isotope evidence in basalts from Hainan Island. *Chin. J. Geochem.* **15**, 1–19.

Zhang J. J., Zheng Y. F. and Zhao Z. F. (2009) Geochemical evidence for interaction between oceanic crust and lithospheric mantle in the origin of Cenozoic continental basalts in east-central China. *Lithos* **110**, 305–326.

Zhang Y., Ren Z. Y. and Xu Y. G. (2013) Sulfur in olivine-hosted melt inclusions from the Emeishan picrites: implications for S degassing and its impact on environment. *J. Geophys. Res.: Solid Earth* **118**, 4063–4070.

Zhou X. H. and Armstrong R. L. (1982) Cenozoic volcanic rocks of eastern China – secular and geographic trends in chemistry and strontium isotopic composition. *Earth Planet. Sci. Lett.* **58**, 301–329.

Zhou P. B. and Mukasa S. B. (1997) Nd, Sr, Pb isotopic, and major- and trace-element geochemistry of Cenozoic lavas from the Khorat Plateau, Thailand: sources and petrogenesis. *Chem. Geol.* **137**, 175–193.

Zou H. B. and Fan Q. C. (2010) U–Th isotopes in Hainan basalts: implications for sub-asthenospheric origin of EM2 mantle endmember and the dynamics of melting beneath Hainan Island. *Lithos* **116**, 145–152.

Zou H. B., Zindler A., Xu X. S. and Qu Q. (2000) Major, trace element, and Nd, Sr and Pb isotope studies of Cenozoic basalts in SE China: mantle source, regional variations, and tectonic significance. *Chem. Geol.* **171**, 33–47.

Associate editor: Andreas Stracke